

CHAPTER 2

Turbulence and transport in mirror geometries in the Large Plasma Device

In this chapter we study turbulence and cross-field particle transport in LAPD mirror configurations. Mirror machines are once again rising in prominence as a candidate for commercial fusion reactors with the advent of highly-funded commercial ventures and high-field high-temperature superconducting magnets [EAB23, FAE24], so development of a functional understanding of cross-field transport in mirrors is imperative. Using the LAPD, multiple mirror ratios from $M = 1$ to $M = 2.68$ and three mirror-cell lengths from $L = 3.51\text{m}$ to $L = 10.86\text{m}$ were examined. Langmuir and magnetic probes were used to measure profiles of density, temperature, potential, and magnetic field. The fluctuation-driven $\tilde{E} \times B$ particle flux was calculated from these quantities. Two probe correlation techniques were used to infer wavenumbers and two-dimensional structure. Cross-field particle flux and density fluctuation power decreased with increased mirror ratio. Core density and temperatures remain similar with mirror ratio, but radial line-integrated density increased. The physical expansion of the plasma in the mirror cell by using a higher field in the source region may have led to reduced density fluctuation power through the increased gradient scale length. This increased scale length reduced the growth rate and saturation level of rotational interchange and drift-like instabilities. Despite the introduction of magnetic curvature, no evidence of mirror driven instabilities interchange, velocity space, or otherwise were observed. For curvature-induced interchange, many possible stabilization mechanisms were present, suppressing the visibility of the instability.

This chapter is largely a copy of my 2025 publication in the Journal of Plasma Physics titled

“Turbulence and transport in mirror geometries in the Large Plasma Device” [tra], with some additions and small changes

2.1 Introduction

Historically, mirror research has prioritized the main issues with mirror confinement: stabilizing the interchange instability, stabilizing velocity-space (loss-cone-driven) instabilities, and minimizing axial electron heat losses. Nevertheless cross-field transport remains an important topic in magnetic-confinement fusion reactor development, in both linear and toroidal geometries. Insight into edge-relevant turbulence, and its coupling to interchange and other mirror-driven instabilities, performed in a basic plasma science device may be useful for a mirror-based reactor. Although not at fusion-relevant core temperatures or densities, the Large Plasma Device (LAPD) operates at conditions similar to the edge of fusion devices and can provide insight into the physical processes in that region. A characterization of edge fluctuations has been undertaken, with emphasis on interpreting these fluctuations within the context of mirror.

Non-classical cross-field particle transport is often caused by low-frequency, large-amplitude fluctuations. These fluctuations are the result of various instabilities. One such process is the "universal" drift instability, which appears in the presence of a density gradient and finite resistivity. Drift wave turbulence and the effect on transport has been extensively studied in the past [Hor99, TFM09]. In the presence of sufficiently high rotation or sheared flow, rotational interchange and the Kelvin-Helmholtz instabilities also contribute or couple to these fluctuations.

Various gradient-, rotation-, and shear-driven instabilities (and suppression of such) have been studied previously in the LAPD experimentally [SCR12, SCR13, Sch13] and in simulations using BOUT, a 3d fluid turbulence code, and an eigenvalue solver [PUC10]. The LAPD has a sufficiently high spontaneous rotation rate that rotation-driven instabilities may be excited without artificial drive. Simulations using BOUT++ [FCU13] have also suggested that a rapidly growing nonlinear instability may dominate over all other linear instabilities.

Imposing a magnetic mirror configuration introduces magnetic curvature. The alignment of the curvature vector with a pressure gradient vector component causes the flute-like interchange instability if no stabilization mechanism is present. This interchange mode could couple to finite k_{\parallel} drift waves. The coupling of drift waves to curvature-induced interchange modes has been studied in toroidal devices such as TORPEX [PBD06, FLM06], where curvature was seen as the driving component for the unstable drift-interchange modes. Drift-like fluctuations have also been observed in the GAMMA-10 mirror [MII91, YMM10]. Flute-like modes and drift waves have been studied in other linear devices, such as Mirabelle [BGB05], where the appearance of flute-like modes or drift waves were controlled by varying the field and limiter diameter.

The rotational interchange and curvature interchange can both be flute-like modes. Rotational interchange (also called the “centrifugal instability”) is driven by the aligned centrifugal force and pressure gradient vectors, but curvature-driven interchange is instead driven by magnetic curvature and is typically referred to as simply the “flute” or “interchange” instability. Rotational interchange [Jas72] has been observed in the LAPD in the past [SCR12, Sch13], and the curvature-driven interchange instability has been observed in many other mirror machines [WV82, FWD83, Pos87].

Biasing or modifying the electrical connection of the plasma with the end wall has proven to be an important actuator in many mirror machines such as TMX-U [HBF84], GAMMA-10 [MII91], and GDT [BLZ03, BBS07, BBC10], and will be utilized on WHAM [EAB23]. Active biasing was not attempted in this study, but the intrinsic rotation and strong electrical connection to the source region may provide a useful analog for edge biasing in other mirror machines.

The LAPD exhibits a high degree of turbulence so it is difficult to identify the dispersion relation of the modes that are present. Nevertheless, the LAPD has good coverage of perpendicular spectra using correlation-plane techniques, and some measure of parallel spectra using the correlation between two axially-separated probes. A space-time spectral characterization of the many instabilities present in this low beta, moderate aspect ratio, gas-dynamic trap regime is attempted.

This goal of this study was to investigate the changes to turbulence and transport in LAPD mirror configurations. Of particular interest were the potential coupling of the interchange instability

with drift waves or other modes, and the effect of the mirror geometry on cross-field particle flux. Presented is a characterization of the observed modes and the effect of introducing a mirror geometry. This paper is organized as follows. Sec. 2.2 discusses the configuration of the LAPD and the diagnostics used. Sec. 2.3 covers the changes seen when imposing a magnetic mirror configuration on profiles, particle flux, drift waves, turbulence, and magnetic fluctuations. Sec. 2.4 explores the changes in 2d (x-y plane) structure. Sec. 2.5 discusses the active and expected instabilities and reasons for their modification. Sec. 2.6 summarizes the study and discusses the requirements for a deeper investigation.

2.2 The experiment and device configuration

2.2.1 The Large Plasma Device (LAPD)

In this study, the plasma was formed using an emissive, 72 cm diameter barium-oxide (BaO) cathode [GPL16a] (mapped to 60 cm in a flat field) and a 72 cm diameter, 50% transparent molybdenum anode that accelerate electrons across a configurable 40 – 70V potential; voltages of 60 and 63V were used in this study. The source has since been upgraded to a lanthanum hexaboride (LaB6) cathode [QGP23a] that enables access to higher-density, higher-temperature regimes, but all the data in this study are from plasma formed by a BaO cathode.

The flexible magnetic geometry of the LAPD was used to construct a variety of magnetic mirror configurations. The discharge current, fill pressure, and other machine parameters were held constant. The typical plasma parameters observed in this study can be seen in table 2.2. Data in several mirror ratios and lengths were collected (see table 2.1) but emphasis is placed on the short cell because the highest mirror ratio possible ($M = 2.68$) with a 500 Gauss midplane field could be accessed and probes were able to be placed outside of the mirror cell. An overview of the axial magnetic field for the the short mirror configurations and probe locations can be seen in fig. 2.1. 2- or 3-cell mirror configurations were also explored but are not examined in this study. All results presented below are from the short mirror cell configuration unless otherwise specified.

2.2.2 Diagnostics

All diagnostics were recorded with a effective sampling rate of 6.25 MHz (16-sample average at 100 MSPS) and a spatial resolution of 0.5 cm. When necessary, averaging over time is done in the approximate steady-state period of the plasma discharge (4.8 to 11.2 ms from the 1 kA trigger signal). Unless otherwise noted, all data presented will be from probes inside the mirror region ($z \approx 7\text{m}$). An example of a raw I_{sat} signal and processing steps can be seen in fig. 2.2. The raw signals are detrended by subtracting the mean across shots to obtain the fluctuations only. FFTs are then taken of these fluctuations for calculating power spectra and cross-correlated quantities. Frequencies above 200 kHz are dominated by electronics and instrumentation noise and thus are also ignored. Fluctuation power profiles can then be constructed.

The data presented were collected in two phases. The first phase ("datarun"), DR1, collected Langmuir probe (I_{sat} and V_f) and magnetic fluctuation ("Bdot") [EPC09] traces. 50 shots were taken at each position for every configuration. The second phase, DR2, was conducted with a similar set of diagnostics focused on temperature measurements (swept and triple probe) and 2d x-y structure. 15 shots were taken at each position, except for Langmuir sweeps with 64 shots. When appropriate, all data for each position were shot-averaged. " I_{sat} " will be used interchangeably with "density" and be presented with units of density (assuming a flat $T_e = 4.5\text{ eV}$ profile).

2.3 Mirror-induced changes

2.3.1 Profile modification

Because the field at the plasma source increases with M , the midplane plasma expands by a factor of \sqrt{M} . The physical locations of the peak fluctuation region – x_{PF} (maximum gradient) – and the cathode radius x_c can be seen in tab. 2.3. This expansion leads to broader plasma profiles and decreased core density but are similar in the core and at x_{PF} when magnetically-mapped to the cathode radius x_c as seen in fig. 2.4. Dips between the core ($x/x_c = 0$) and the peak fluctuation

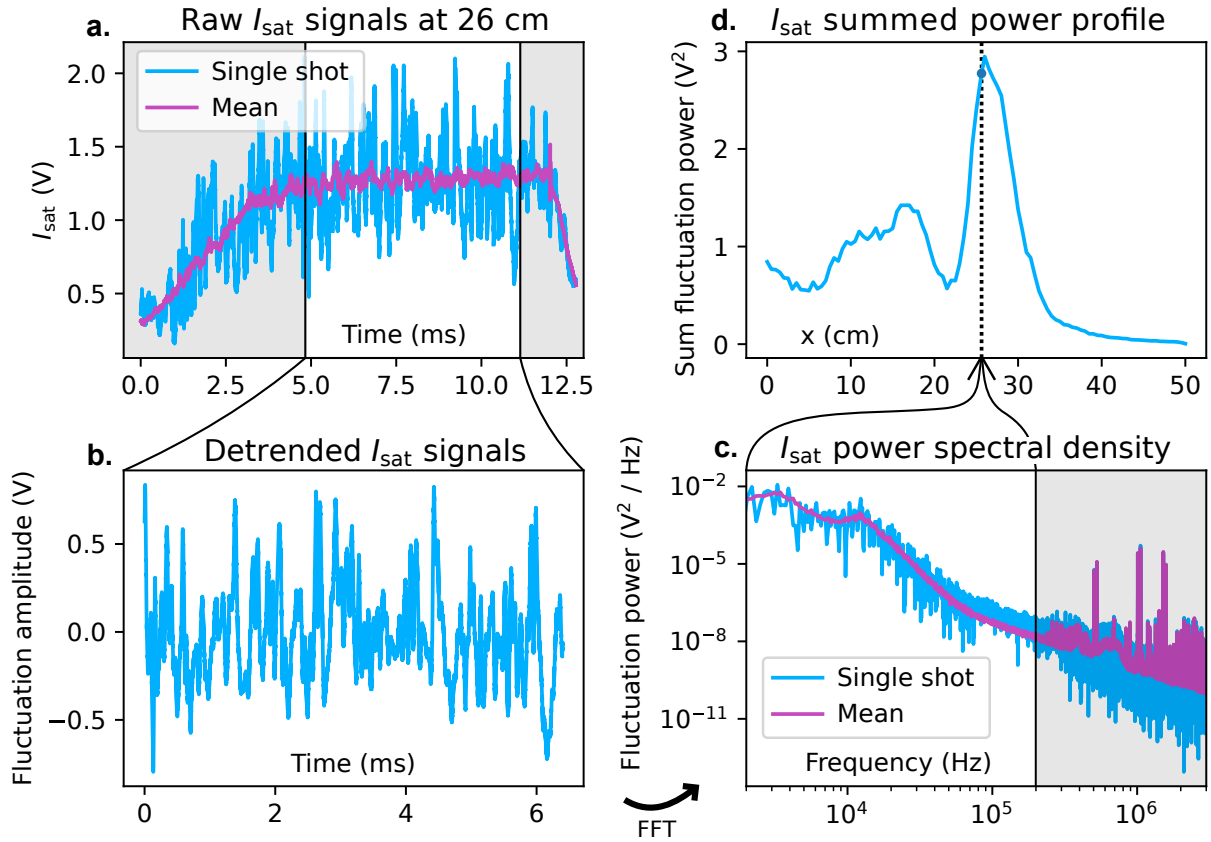


Figure 2.2: Raw data and basic processing steps for LAPD probe diagnostics as demonstrated by an I_{sat} trace from a DR1, $M = 1$ mirror at 26 cm. Data are truncated from 4.8 to 11.2 ms (a) and detrended (b). Power spectral density is calculated (c), and a power profiles can be constructed (d). The shaded regions are excluded from this analysis.

| | | | | |
|-----------------------------|--------------------------|-------------------------|----------------------|---------------------|
| Cathode radius (M=1) | x_c | 30 | | cm |
| Machine radius | R | 50 | | cm |
| Plasma length | L | ~ 17 | | m |
| Primary species | | He-4 1+ | | |
| Electron-helium mass ratio | | 1.37×10^{-4} | | |
| Neutral pressure | | $6 - 20 \times 10^{-5}$ | | Torr |
| Quantity | | Core | $x = x_{\text{PF}}$ | Unit |
| Density | n_e | 1.25×10^{12} | 0.6×10^{12} | cm^{-3} |
| Ion temperature | T_i | ~ 1 | | eV |
| Electron temperature | T_e | 4 | 5 | eV |
| Beta (total) | β | 9×10^{-4} | 6×10^{-4} | |
| Midplane magnetic field | B_{mid} | 500 | | G |
| Plasma freq | Ω_{pe} | 10 | 7.1 | GHz |
| Ion cyclotron freq | Ω_{ci} | 200 | | kHz |
| Electron cyclotron freq | Ω_{ce} | 1.4 | | GHz |
| Debye length | λ_D | 0.013 | 0.021 | mm |
| Electron skin depth | λ_e | 30 | 43 | mm |
| Ion gyroradius | λ_{ci} | 5.8 | | mm |
| Electron gyroradius | λ_{ce} | 0.13 | 0.15 | mm |
| Ion thermal velocity | \bar{v}_i | 6.94 | | km/s |
| Electron thermal velocity | \bar{v}_e | 1190 | 1330 | km/s |
| Sound speed | c_s | 13.0 | 13.9 | km/s |
| Alfvén speed | v_a | 446 – 1140 | –1620 | km/s |
| Ion sound radius | ρ_s | 65 | 69 | mm |
| Ion-ion collision freq | ν_{ii} | 730 | 380 | kHz |
| Electron-ion collision freq | ν_{ei} | 6.77 | 2.59 | MHz |
| Electron collision freq | ν_{ee} | 9.57 | 3.66 | MHz |
| Ion mean free path | $\lambda_{i,\text{mfp}}$ | 26 | 50 | mm |
| Electron mean free path | $\lambda_{e,\text{mfp}}$ | 175 | 512 | mm |
| Spitzer resistivity | η | 192 | 146 | $\mu\Omega\text{m}$ |

Table 2.2: LAPD machine information and plasma parameters in the core and peak-fluctuation region ($x = x_{\text{PF}}$) at the midplane in this study. Dashed quantities are assumed to be identical to core quantities.

| Mirror ratio | 1 | 1.47 | 1.90 | 2.30 | 2.68 |
|---------------|----|------|------|------|------|
| Scale factor | 1 | 1.21 | 1.38 | 1.52 | 1.64 |
| x_c (cm) | 30 | 36 | 41 | 45 | 49 |
| x_{PF} (cm) | 26 | 32 | 36 | 40 | 43 |

Table 2.3: x_c and x_{PF} locations for each mirror ratio when scaled by the expected magnetic expansion.

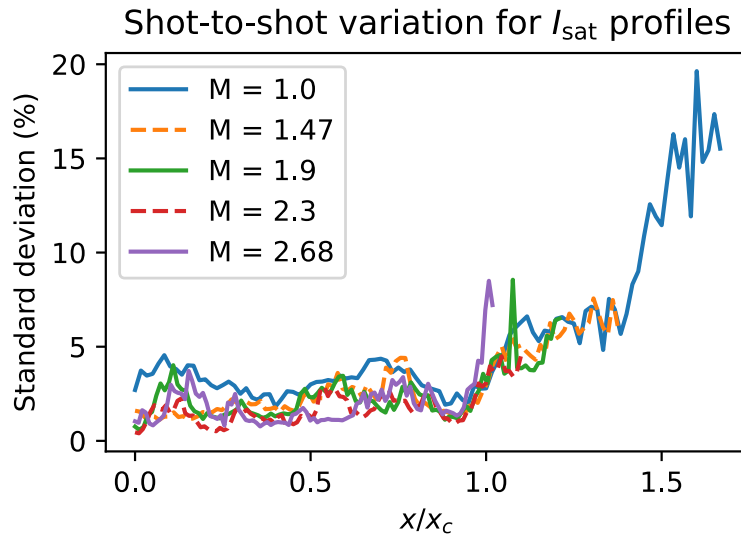


Figure 2.3: Shot-to-shot variation of I_{sat} profiles

region ($x = x_{PF}$) are seen, but fluctuation power from this region ($x/x_c = 0.5$ to 0.7) is not significant (fig. 2.8) so this region is not the focus of this study. The line-integrated density as measured by a 56 GHz heterodyne interferometer increases up to $\sim 35\%$ from the $M=1$ case of $\approx 8 \times 10^{13} \text{ cm}^{-2}$ (fig. 2.5) but does not increase past a mirror ratio of 2.3.

The error of on the I_{sat} profiles as represented by the standard deviation (scaled by the time-averaged profiles) can be seen in fig. 2.3. The error is relatively small and should not play a factor in our analysis – rarely are differences between quantities of the different mirror ratios that small.

Discharge power increases only slightly (3%) at higher mirror ratios suggesting negligible impact on density. Langmuir sweeps and triple probe measurements of T_e (DR2) show slightly (less than 25%) depressed core and slightly elevated edge T_e with increasing mirror ratio (fig. 2.6) but otherwise remains unaffected. The temperature affects I_{sat} measurements through the $\sqrt{T_e}$ term so small changes are insignificant. The low temperatures indicate that the plasma is collisional given the length scales of the system (as seen in table 2.2) and isotropic. Plasma potential decreases across the plasma (fig. 2.7) when the mirror ratio exceeds 1.9. This drop in plasma potential may be caused by the grounding of the anode to the wall, which should begin at $M = 1.93$ given the 72 cm anode and 100 cm vessel diameters. The reason for the local minimum in the $M=2.68$ is unknown. This potential profile creates a sheared $\mathbf{E} \times \mathbf{B}$ velocity profile (fig. 2.7) limited to 500 m/s in the core and exceeding ~ 3 km/s at the far edge. The flow does not exceed 4% of the sound speed (tab. 2.2) in the core or gradient ($x = x_{PF}$) region. The mirror ratio does not appear to significantly alter azimuthal flow. The floating potential (Vf) profile also exhibits similar behavior to the plasma potential (fig. 2.7), but is modified by the presence of primary electrons.

2.3.2 Reduced particle flux

The density fluctuation power peaks at the steepest gradient region ($x_{PF} = x/x_c \sim 0.88$) as expected as seen in fig. 2.8. x_{PF} occurs at nearly the same magnetically-mapped coordinate for each mirror ratio. These density fluctuations are a large driver of changes in the cross-field particle flux (eq. 2.1). Vf fluctuations also peak at the same location, but the total power across mirror ratios are similar and, relative to density fluctuations, much lower in the core. Core density fluctuations below 2 kHz are substantial in the core at lower mirror ratios, possibly caused by hollow profiles, nonuniform cathode emissivity, or probe perturbations, but are outside the scope of this study.

A spectral decomposition technique is used to calculate the time-averaged particle flux [Pow74] as seen in fig. 2.9:

$$\Gamma_{\tilde{E} \times B} = \langle \tilde{n} \tilde{v} \rangle = \frac{2}{B} \int_0^\infty k(\omega) \gamma_{n\phi}(\omega) \sin(\alpha_{n\phi}) \sqrt{P_{nn}(\omega) P_{\phi\phi}(\omega)} d\omega \quad (2.1)$$

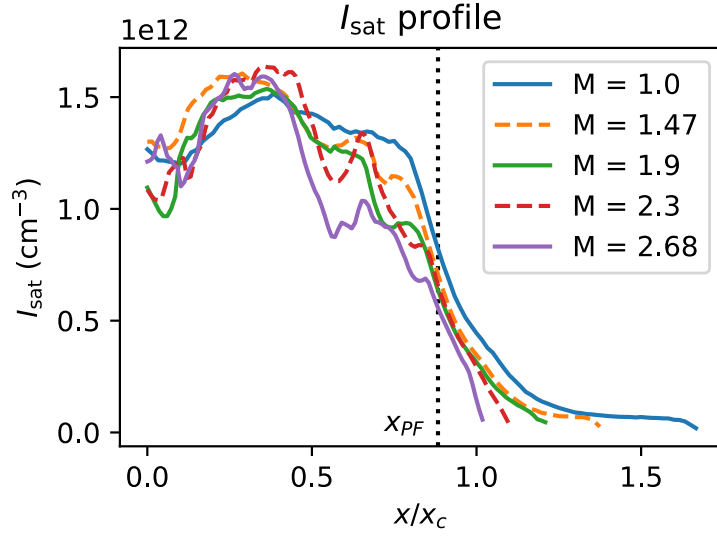


Figure 2.4: Midplane I_{sat} profile, shot-averaged and time-averaged from 4.8 to 11.2 ms (assumed of $T_e = 4.5$ eV based on triple probe and Langmuir sweep measurements). Effective area was calibrated using a nearby interferometer. Profile shape remains similar in the core and gradient region when mapped to the cathode radius x_c . The dips in profiles at higher M below $x = x_{\text{PF}}$ are of unknown origin and are not the focus of this study. Shot-to-shot variation is less than 5% for $x \leq 0.95x_c$ and less than 9% for $x \leq 1.4x_c$ for all cases.

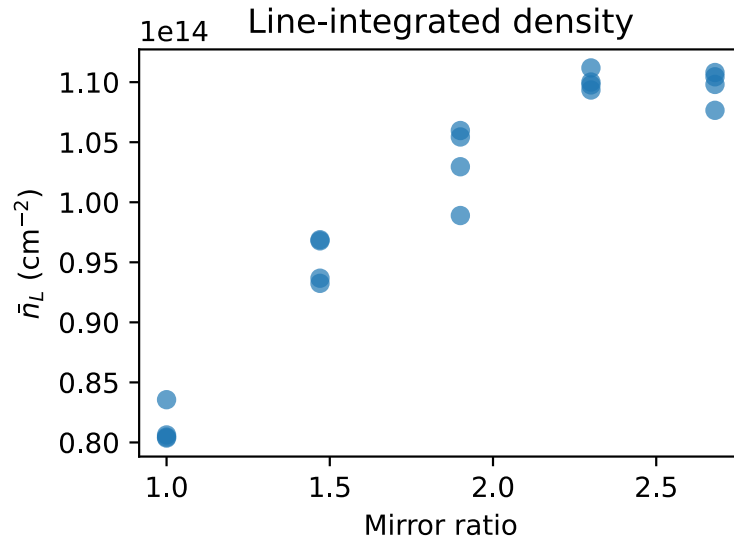


Figure 2.5: Line-integrated density as measured by a 56 GHz heterodyne interferometer as a function of mirror ratio, taken from four discharges for each mirror configuration. Density increases up to a mirror ratio of 2.3 where it appears to level off. The interferometer is located in the mirror cell bad-curvature region at 9.59m, 1.3m closer to the cathode from the midplane.

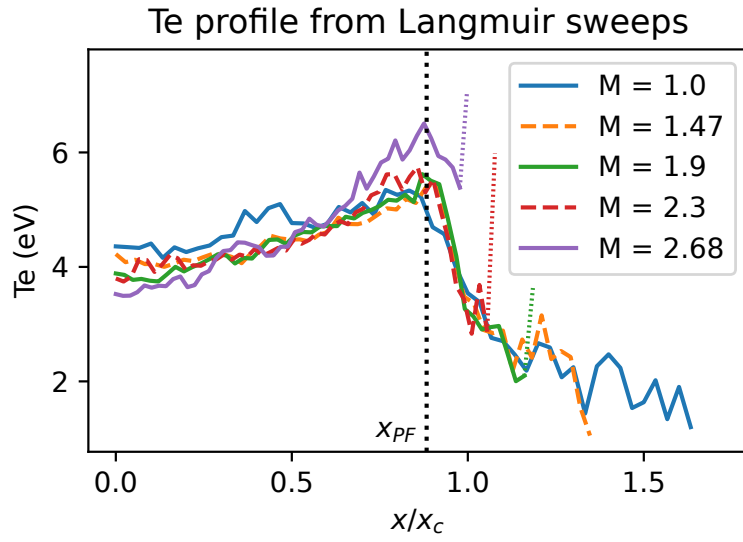


Figure 2.6: T_e from Langmuir sweeps (DR2) at the midplane. Triple probe results are nearly identical. The increased temperatures directly at the plasma edge, indicated by dotted portions of the curves, are likely artifacts caused by sheath expansion in lower densities. Changes in mirror ratio lead to at most 25% change in T_e . The plasma is collisional and isotropic.

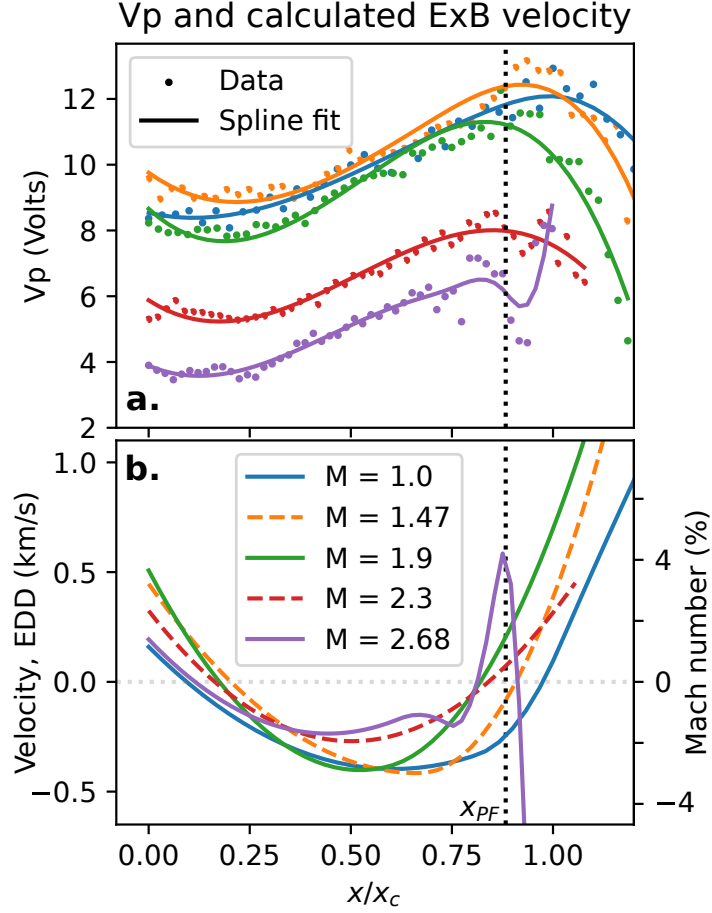


Figure 2.7: Plasma potential (a) and derived $\mathbf{E} \times \mathbf{B}$ velocity profiles (b) from Langmuir sweeps at the midplane. $x/x_c > 1.2$ has been excluded from the graph for greater clarity in the core and gradient region. The electric field was calculated by taking the gradient of the spline-smoothed plasma potential profile. The Mach number (in percent) is calculated using the approximate sound speed evaluated at $x = x_{PF}$ (tab. 2.2). The overall structure of the flows does not appreciably change when mirror ratio is varied.

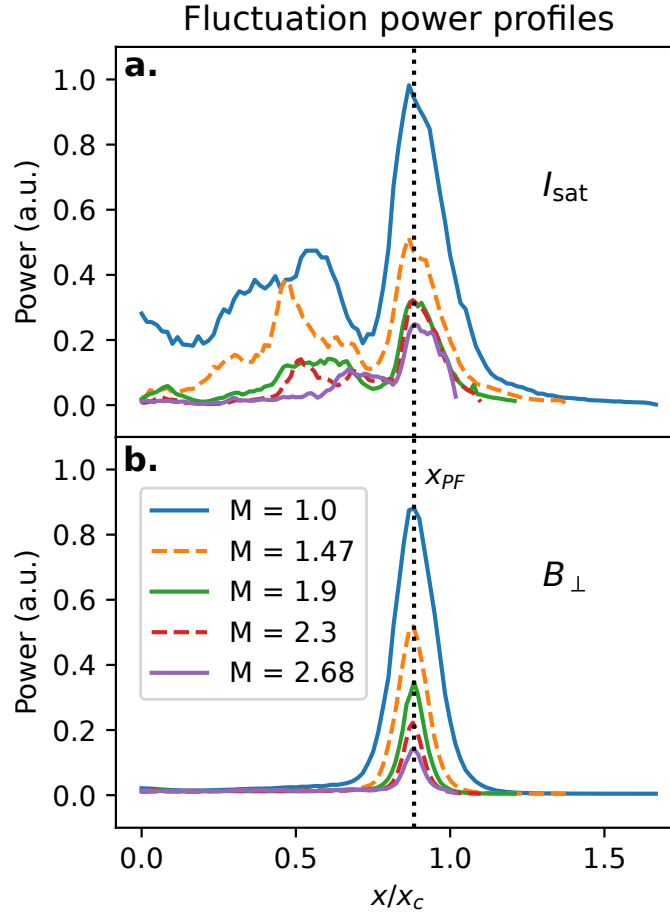


Figure 2.8: I_{sat} (a) and B_{\perp} (b) fluctuation power profiles for signals 2 kHz and up at $z=8.3\text{m}$ (midplane) and $z=7.7\text{m}$, respectively. The lower frequency components in I_{sat} are associated with bulk profile evolution, dominate the core region, and are not the focus of this study.

where k is the azimuthal wavenumber, γ is the coherency, α is the cross-phase, and P the power spectrum. This method is more robust than the naive time-integration of $n(t)\tilde{E}(t)$ because it accounts for the coherency of the density-potential fluctuations. This representation also enables inspection of each contributing term in the event of surprising or problematic results. A plot of the I_{sat} -Vf phase can be seen in fig. 2.10. The flattened particle flux in the core is likely caused by primary electrons emitted by the cathode. These electrons have long mean free paths (greater than a few meters) and sample fluctuations along the length of the machine, mixing the phases of these fluctuations. Since floating potential is set by the hotter electron population, the measured Vf fluctuations are no longer related to the local plasma potential fluctuations of a wave by bulk T_e [CM09]. These primary electrons have a significant effect in the core within the region mapped to the cathode $x \lesssim x_c$. I_{sat} fluctuations are not affected.

Azimuthal wave number is measured by two Vf probe tips 0.5 cm apart. This wavenumber estimation technique yields good agreement with correlation plane measurements (fig. 2.31). Note that \tilde{E} is not directly measured – it is instead calculated through the $k(\omega)\sqrt{P_{\phi\phi}(\omega)}$ terms. The $\tilde{E} \times B$ particle flux clearly decreases with mirror ratio; most of this decrease is attributed to the decrease in density fluctuation power. The particle flux for each mirror ratio was normalized to the $M = 1$ case via the plasma circumference to compensate for the increased plasma surface area at the same magnetically-mapped coordinate x/x_c . This particle flux is on the order of Bohm diffusion $D_B = \frac{1}{16} \frac{T_e}{B} \approx 6.25 \text{m}^2 \text{s}^{-1}$ as observed in other transport studies [MCT07].

T_e profiles and fluctuations may affect particle fluxes but measurements of both were not taken in the same datarun; nevertheless, a quantification of the effect of T_e on particle flux is attempted. T_e fluctuations affect I_{sat} -based density measurements through the $T_e^{-1/2}$ term, and triple probe and Langmuir sweep T_e measurements suggest that temperature gradients have a negligible impact. A naive incorporation of temperature fluctuation data from DR2 into particle fluxes from DR1 suggest that cross-field particle flux may be underestimated by up to 50% via the I_{sat} temperature term, but the trend and relative fluxes across mirror ratios remain unchanged. Such a naive incorporation should be treated with suspicion because of the sensitive nature of the flux with respect to the

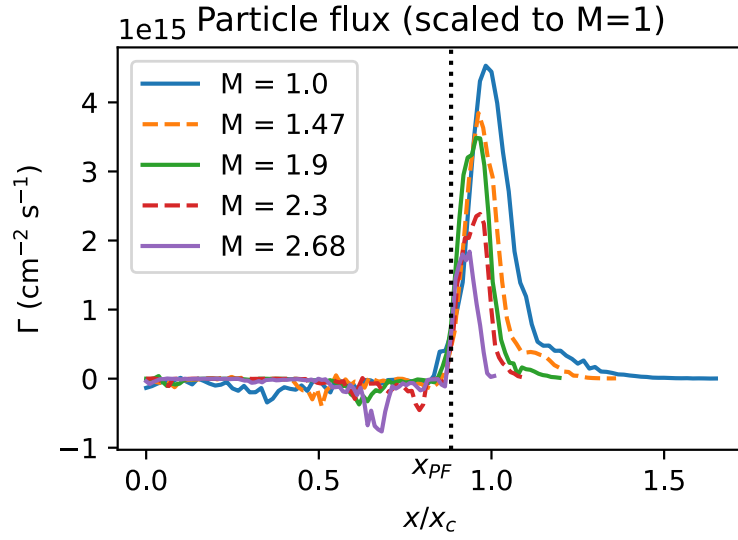


Figure 2.9: Cross-field, $\tilde{E} \times B$ fluctuation-based particle flux (calculated using eq. 2.1) with respect to mirror ratio. A monotonic decrease in particle flux is observed with increasing mirror ratio at the midplane. Particle flux is normalized by plasma circumference to the $M = 1$ case to account for the geometry-induced decrease in particle flux caused by a larger-diameter plasma.

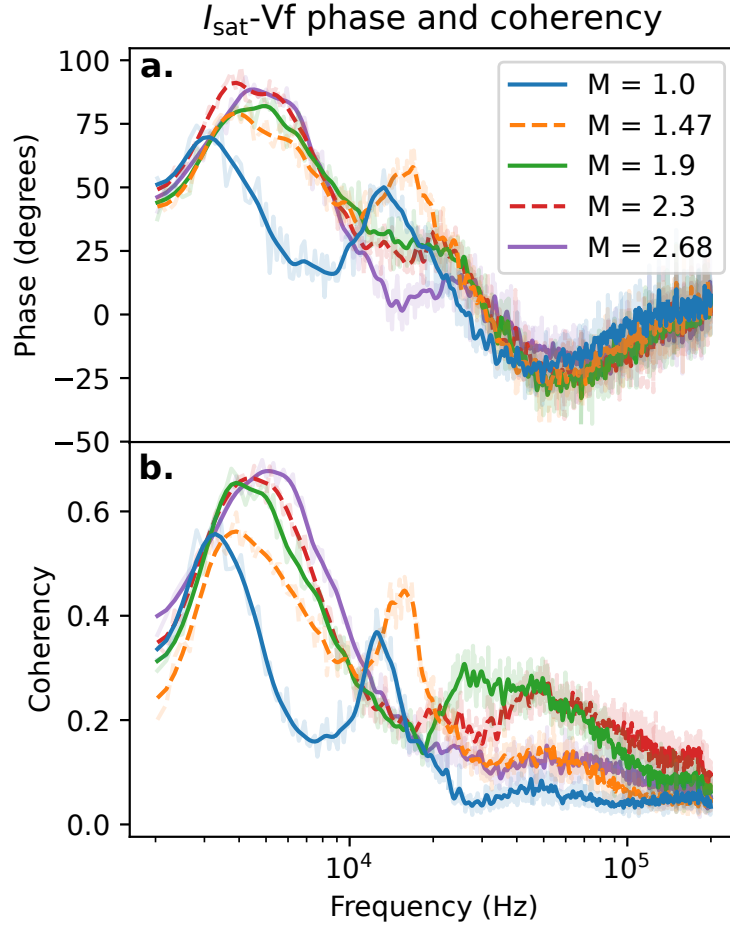


Figure 2.10: Phase (a) and coherency (b) of I_{sat} current and V_f near x_{PF} at the midplane, smoothed. Positive phase means I_{sat} leads V_f . Peaks in coherency occur between 3-5 kHz and at the drift-Alvén wave peaks between 12 and 25 kHz. These coherency peaks tend to have larger phase shifts than other nearby frequencies.

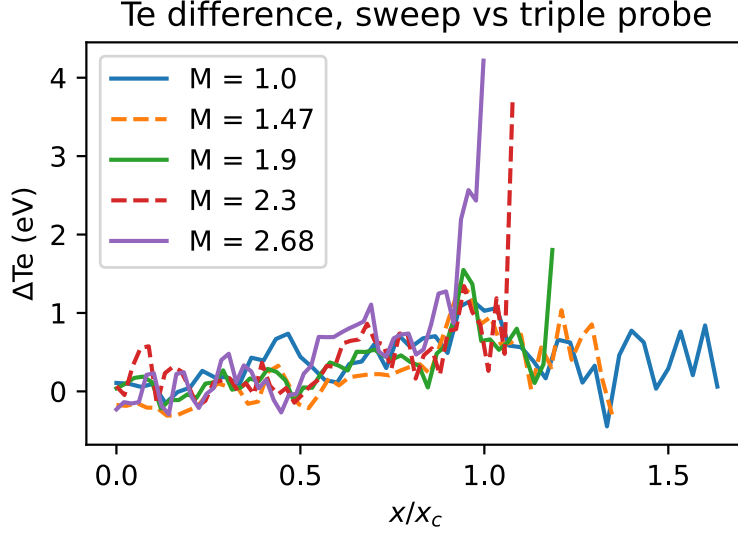


Figure 2.11: Difference between swept and triple probe temperature measurements. The triple probe appears to slightly underestimate the temperature and temperature gradient.

gradient and the differences in profiles between DR1 and DR2. These difference in profiles made be caused by cathode condition, deposits on the anode, or a different gas mix and are difficult to account for.

2.3.3 Compensating for the Te profile

Electron temperature (T_e) compensation for the I_{sat} measurement can be done in several ways. One way is to account for the average temperature (i.e., steady state) when calculating the density from I_{sat} . T_e can be gathered from triple probe or swept measurements. Triple probe measurements are generally less reliable than swept probe measurements. The difference between swept and triple probe T_e measurements can be seen in fig. 2.11. The two techniques have roughly good agreement, though the triple probe appears to slightly underestimate the temperature. The spikes in the edge are likely from sheath expansion of the probe in the swept measurements (see fig. 2.6).

T_e fluctuations can affect I_{sat} fluctuation measurements through the $\sqrt{T_e}$ term. In this case, T_e

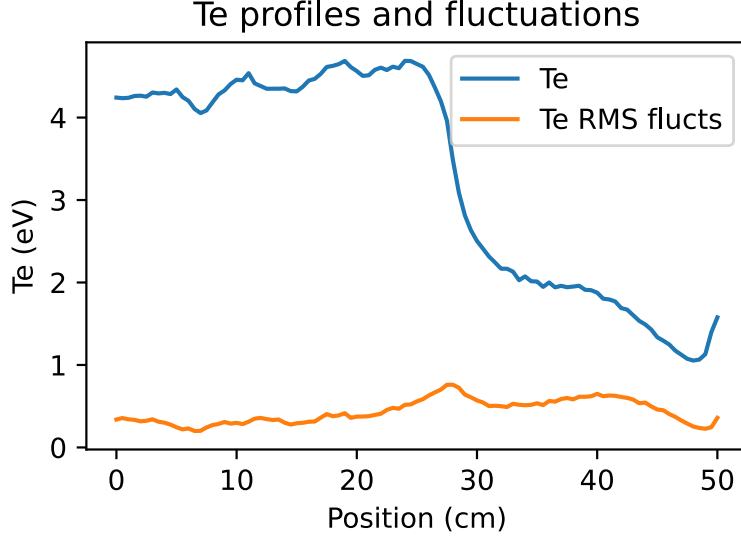


Figure 2.12: Te and Te fluctuation profiles from the triple probe. RMS electron temperature fluctuations are not particularly large.

measurements are difficult to compensate for in DR1 because of the changes in profiles between DR1 and DR2, so the Te fluctuations were included by finding the ratio in DR2 of I_{sat} fluctuations before and after including these Te fluctuations. This ratio was then applied to DR1. The issue of mismatched profiles still persists but this method allows for changes in fluctuation power between the two datarun sets. In general, \tilde{T}_e/T_e fluctuations are at most than 30% (near the edge), and much lower in the core seen in fig. 2.12.

This Te compensation becomes particularly important when calculating the I_{sat} profile gradients which is needed when calculating the diffusivity. A calculation of the diffusivity scaled to the Bohm diffusivity $D_B = \frac{1}{16} \frac{T}{eB}$ can be seen in fig. 2.13. This calculation uses the particle flux calculated earlier (in the paper) and tanh fit on the density profile for a density smooth gradient. In general, mirror ratios higher than two have a lower diffusivity. When the particle flux is compensated for Te fluctuations, the temperature profile used in for the Bohm diffusion coefficient, and the density profile is smoothed convoluting a $\sigma = 2$ cm gaussian, the diffusion coefficient relative to D_B are roughly 2.5 times greater, seen in fig. 2.14. The trend, however, remains relatively

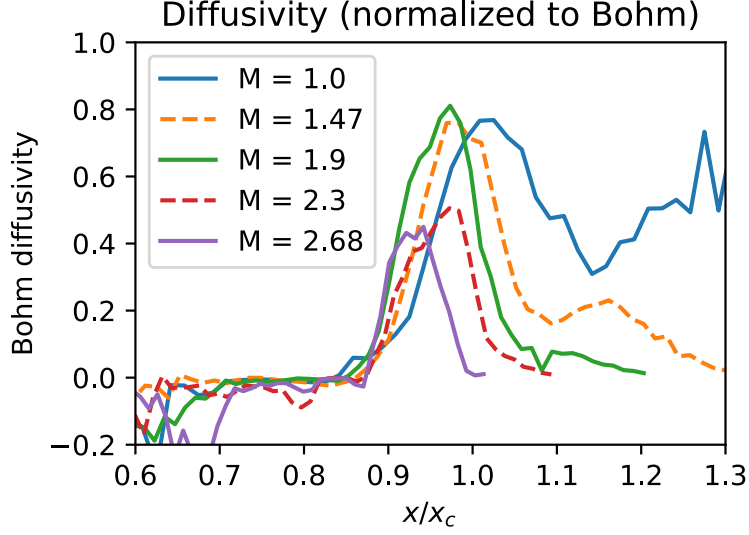


Figure 2.13: Diffusivity relative to D_B using a tanh fit for the density profile and the particle flux measurement assuming a constant T_e of 4.5 eV across the profile.

the same: higher mirror ratios tend to have a lower diffusivity. The impact of different profile smoothing methods on the density gradient can be seen in fig. 2.15.

2.3.4 Drift waves

The I_{sat} fluctuation power spectra in the region of peak power $x \sim x_{\text{PF}}$, also where the density gradient is strongest, can be seen in fig. 2.16. Notably, the fluctuation peaks shift to higher frequencies and decrease in total fluctuation power. The shift in frequency may be the Doppler shift caused by the change $\mathbf{E} \times \mathbf{B}$ plasma rotation seen in fig. 2.7 at the location $x/x_c \approx x_{\text{PF}}$. The shift in frequency is somewhat smaller than what would be expected from the field line-averaged increase in Alfvén speed at the longest possible wavelength. The phase angle of I_{sat} and V_f provides insight into the nature of the driving instability. Including a nonzero resistivity η in the drift wave leads to a small phase shift δ between density and potential. This phase shift δ in a collisional plasmas is on the order of $\delta \approx \omega v_e / k_{\parallel}^2 \bar{v}_e^2$ [Hor99]. Estimating this quantity using measured and

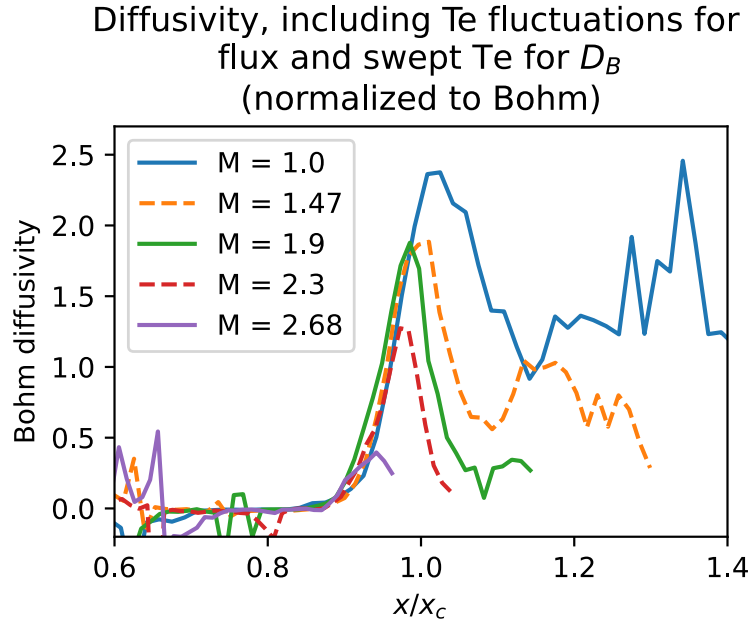


Figure 2.14: Diffusivity with Te compensation relative to D_B . The particle flux is compensated for Te fluctuations, and the swept-probe temperature profile is used for Te. The diffusivity is around 2.5 times higher than without compensation, but the trend remains similar.

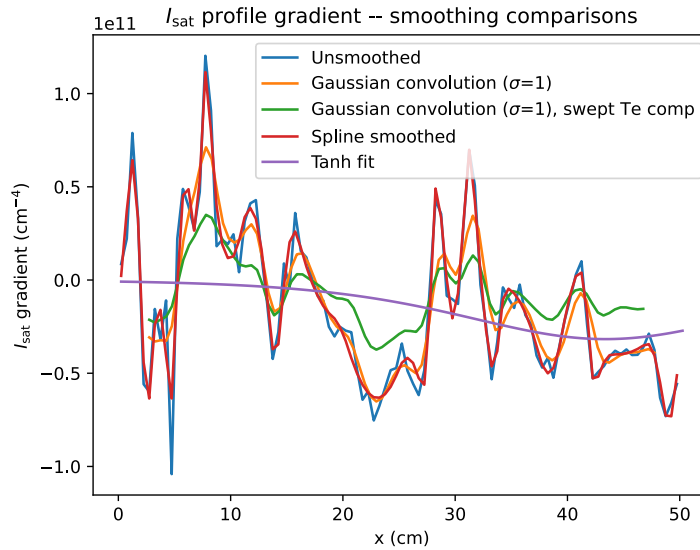


Figure 2.15: I_{sat} gradients under varying profile smoothing methods

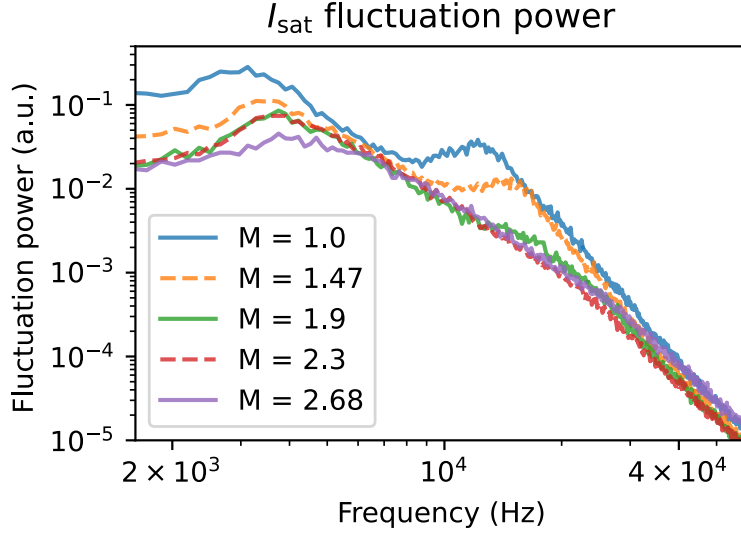


Figure 2.16: I_{sat} (density) fluctuation power averaged over a 1 cm region around x_{PF} at the mid-plane. The fluctuation power is largely featureless below 2 kHz and beyond 40 kHz aside from electronics noise.

typical values ($k_{\parallel} = 0.18$ rad/m, $\bar{v}_e = 1300$ km/s, $v_e = 3.7$ MHz, $\omega = 12$ kHz) yields a substantial phase shift of $\delta \approx 46^\circ$, which roughly agrees with the phase shifts in fig. 2.10, though the implied increased phase shift at higher frequencies does not agree with measurements. As seen in fig. 2.10, the phase shift between I_{sat} and V_f fluctuations are larger below 10 kHz, implying the presence of additional modes beyond or significant modification of resistive drift wave fluctuations. The phase difference between two V_f probes, 3.83 m apart, was used to calculate the parallel wavelength $\frac{2\pi}{\lambda} = k_{\parallel} = \phi_{Vf1, Vf2}/\Delta z$ assuming the wavelengths are greater than 7.66 m. The two probes mapped to the same field line only in the $M = 1$ configuration, so parallel wavenumbers are available only for the flat case. Parallel wavenumbers are theoretically calculable from 2d correlation planes but the coherency dropped dramatically when a mirror geometry was introduced. A 34 m wavelength mode likely contributes to the measured k_{\parallel} from 3 to $\gtrsim 10$ kHz (fig 2.17). Drift waves are long-wavelength modes so coherent density and potential fluctuations along the flux tube are expected. The coherency is a measure of similarity of the spectral content of two signals, in this case V_f

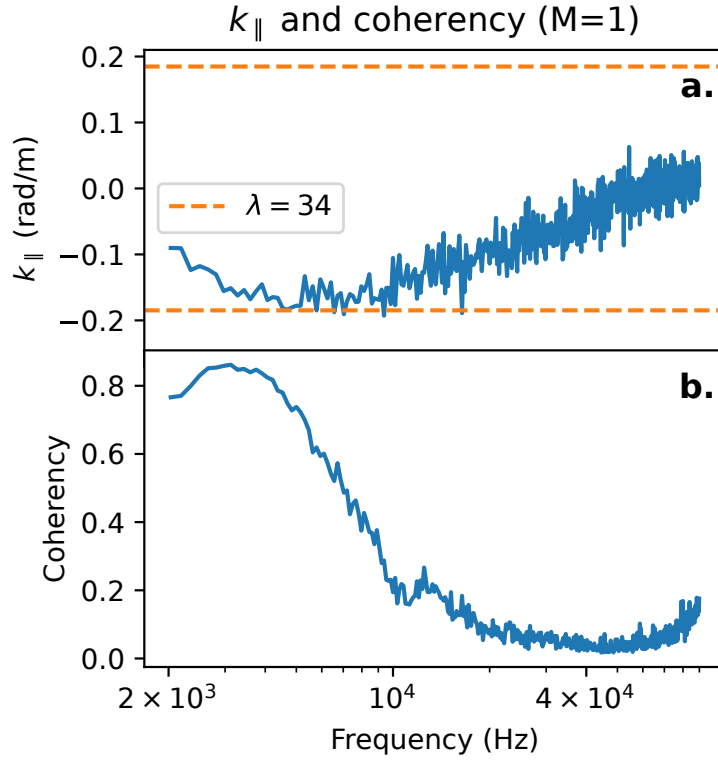


Figure 2.17: k_{\parallel} (a) and coherency γ (b) as a function of frequency. Only results from the $M = 1$ case are available, but it is clear that there are long ($\gtrsim 34$ m) wavelength modes at 3 and 12 kHz. The probes used for calculating k_{\parallel} were located at the midplane ($z=8.31$) and $z=12.14$ m, 3.83 m apart.

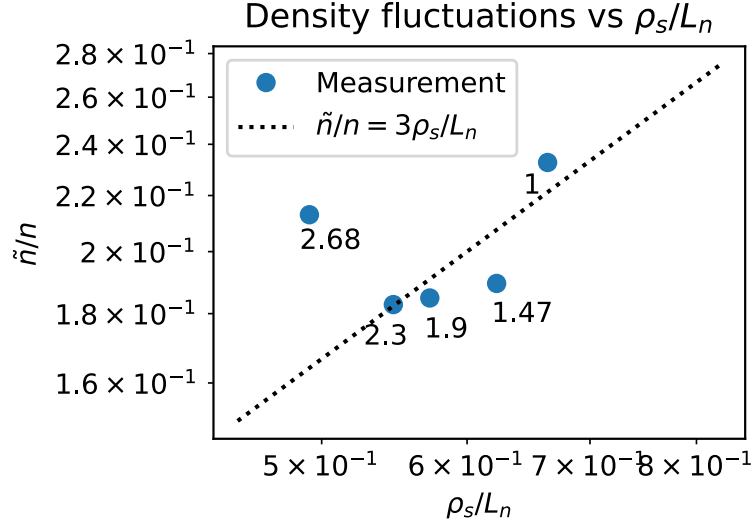


Figure 2.18: Normalized density fluctuations vs ρ_s/L_n . The measured values fall close to the $\tilde{n}/n = 3\rho_s/L_n$ line which is consistent with theory.

probes 1 and 2. The coherency is defined as $\gamma = \frac{|\langle P_{1,2} \rangle|}{\langle |P_{1,1}|^2 \rangle \langle |P_{2,2}|^2 \rangle}$ where $P_{x,y}$ is the cross-spectrum between signals x and y and the angle brackets $\langle \rangle$ denote the mean over shots. The coherency between the two Vf probes drops off with increasing frequency, with a slight bump at around 12 kHz. There are several candidates for the driving mechanism of the 3-5 kHz mode, but the 12 kHz mode is most likely a drift-Alfvén wave.

Drift wave theory[Lie85] suggests that the normalized density fluctuation level \tilde{n}/n should fall near $3-10 \rho_s/L_n$. A plot of this relation using experimental data can be seen in fig. 2.18. However, comparison of \tilde{n}/n with $1/(k_y L_n)$ show that the normalized density fluctuations are about an order of magnitude too small for the $1/(k_y L_n)$ observed which is unexpected and this conflict has not been able to be resolved in this study.

Another issue with this drift-wave interpretation of results is that the electron thermal diffusion along the field line is too high. The plasma must be collisional enough that thermal equilibrium is guaranteed (i.e., the temperature is Maxwellian), but if the collision rate is too high then thermal

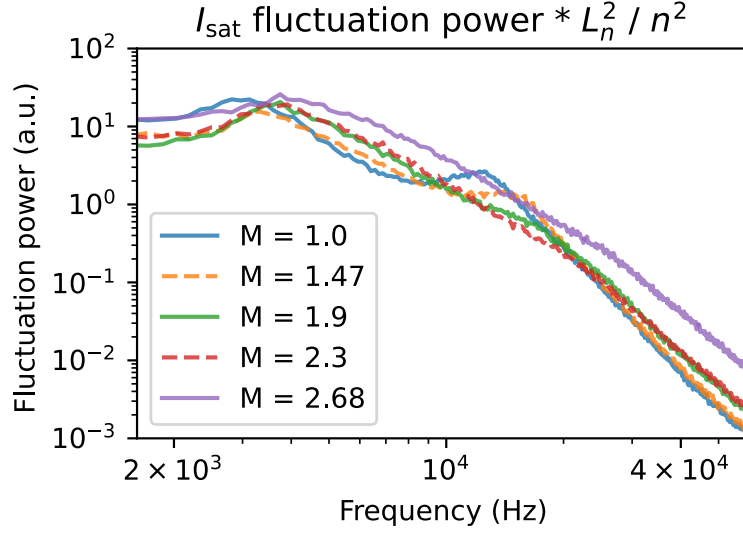


Figure 2.19: I_{sat} fluctuation power when scaled by the square of the gradient scale length and the squared density. We expect this value to be constant (assuming the same k_{\perp}).

gradients can develop along the field line[Go195]. This condition on thermal diffusivity condition for the drift wave ω and k_z is $\omega \ll k_z^2 v_{e,th}^2 / \nu_{ei}$. Plugging in values from the experiments yields frequencies at least 5 times greater than mandated by the diffusivity condition and the condition is violated. This condition violation may be responsible for the odd phase shifts seen between the density and potential fluctuations.

In saturated drift wave turbulence, the normalized density fluctuation amplitude is expected to scale with the gradient scale length L_n , so the fluctuation power then scales with L_n^2 . A plot of this can be seen in fig. 2.19. This assumes the same k_y , but as mentioned earlier, that scaling and the relationship in general is not consistent with theoretical predictions for saturated drift wave turbulence.

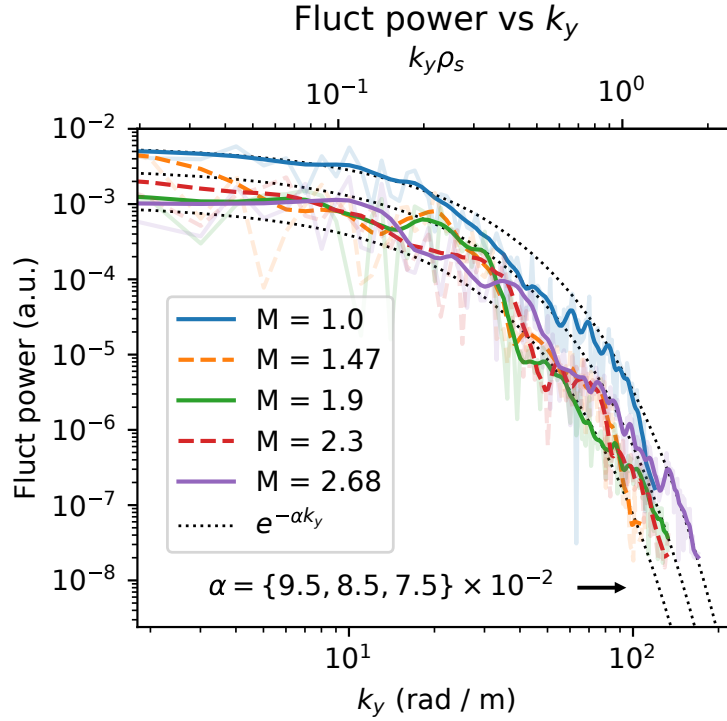


Figure 2.20: Fluctuation power summed for each k_y for frequencies up to 100 kHz, smoothed. The contribution to fluctuation power is negligible past 100 kHz. The fluctuation power decreases substantially when a mirror configuration is introduced, but no trend is seen otherwise and the k_y spectra remain exponential. Note the logarithmic scale.

2.3.5 Turbulence modification

The wavenumber-power relation in fig. 2.20 shows decreased fluctuation power when a mirror configuration is introduced. However, there is no discernible trend when the mirror ratio is increased further. The exponential nature of the curve also remains unchanged. The greatest decrease in fluctuation power occurred in low and high k_y 's, around 10 and 70 rad/m. The shape of the power- k_y curves follow an exponential distribution, and is inconsistent with a 2d drift-wave turbulent cascade (Wakatani Hasegawa k^{-3}) [WH84]. The steep dropoff in fluctuation power with k_y suggests that higher-wavenumber fluctuations do not have a significant effect on transport.

Previous simulations in a flat field [Fri13] predicted frequency and wavenumber spectra that can be fit with many power laws or exponentials, but the data presented here (figs. 2.16, 2.21, 2.20) appear to follow an exponential relationship within measurement variation.

Turbulence measurements can be directly compared to theoretical predictions and other devices, summarized by Liewer [Lie85]. For saturated drift wave turbulence, one expects the normalized fluctuation level $\tilde{n}/n \sim 1/\langle k_\perp \rangle L_n$, where k_\perp is some typical wavenumber. The power-weighted k_y (calculated from fig. 2.20) was approximately 15 rad/m, which is an order of magnitude too small to satisfy this relationship. \tilde{n}/n scaling with ρ_s/L_n , however, is roughly consistent with drift wave turbulence level saturation: the latter is ≈ 3 times larger. These comparisons suggest that the large, low frequency fluctuations (~ 3 kHz, which had even smaller k_y) may have a drift wave turbulence component but are dominantly driven by other instabilities. No trend is seen in ρ_s/L_n and $1/k_y L_n$ when mirror ratio was varied.

Core fluctuations appear to decrease dramatically as seen in the I_{sat} fluctuation power (fig. 2.8). The I_{sat} decorrelation time increases from ~ 0.7 ms for $M = 1$ to ~ 2.5 ms for $M = 2.68$. At $x = x_{PF}$, decorrelation times for all mirror ratios remained at 0.2 ms.

2.3.6 Magnetic fluctuations

The perpendicular magnetic fluctuation (B_\perp) component of the drift-Alfvén wave can be seen in fig. 2.21. These B_\perp fluctuations are spatially and spectrally coincident with the electrostatic fluctuations (fig. 2.16). Drift-Alfvén waves have been studied in the LAPD in the past [MM97, VG06]; strong coupling is observed for $\beta_e > m_e/m_i$ which is satisfied in this study. The Alfvén speed $\omega/k_\parallel = v_A = B/\sqrt{4\pi nM}$ (given $\omega \ll \Omega_{ci}$) when averaged over the entire column ranges from ~ 450 to ~ 1600 km/s. A k_\parallel corresponding to a wavelength $\lambda = 34$ m roughly falls within the bound established by the kinetic and inertial Alfvén wave dispersion relations at the frequency peaks observed at $x \sim x_{PF}$ seen in fig. 2.21. The lengthening of field lines caused by curvature accounts for at most 10% of the change in frequency.

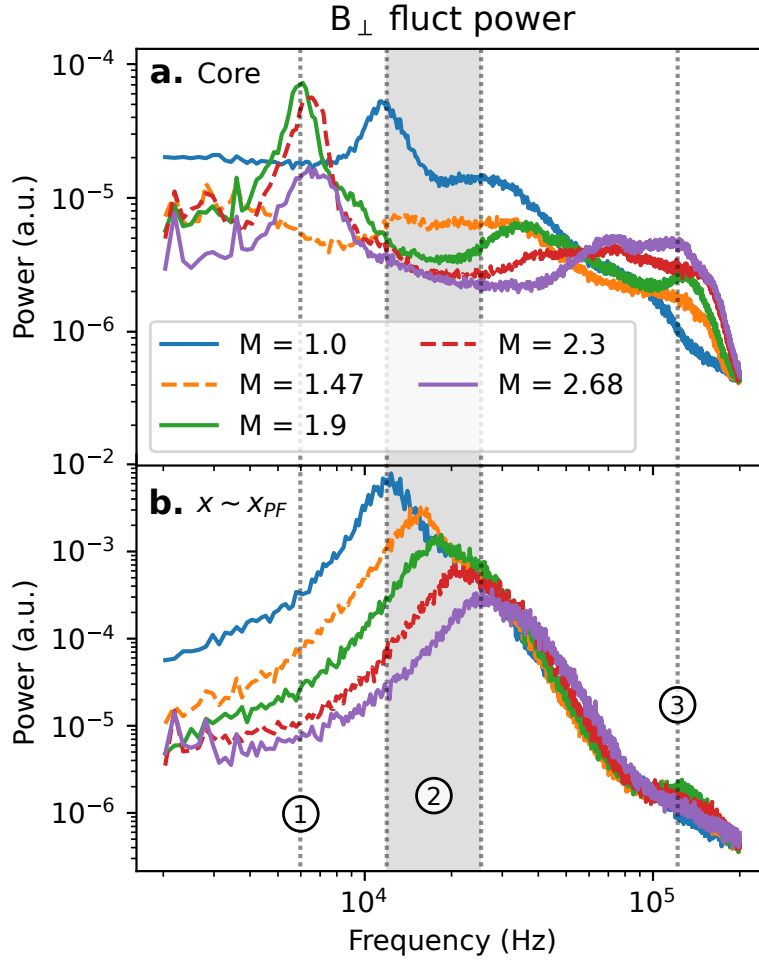


Figure 2.21: B_{\perp} fluctuation power averaged at the core from 0 to 3 cm (a) and around the peak fluctuation point ($x \sim x_{PF}$) (b). Fluctuation power decreases across the board with mirror ratio except for core frequencies close to Ω_{ci} . Peaks around 10 – 30 kHz at x_{PF} are consistent (region 2) with drift-Alfvén waves and the near-cyclotron frequency features in the core may be resonating Alfvén waves created by the magnetic mirror. Frequencies below 2 kHz and dominated by instrumentation noise and thus excluded.

The spatial extent of the B_{\perp} features identified in fig. 2.21 are plotted in fig. 2.22. Feature 1 at ≈ 6 kHz shows increased fluctuation amplitudes at $x = 0$ for mirror ratios 1.9 and above, but for $M = 1$ and $M = 1.47$ there is no increase in fluctuation power. A similar feature, but at a much smaller level, is observed in I_{sat} fluctuation power in the core as well. This core feature may be caused by the hole in the core seen in the I_{sat} profile (fig. 2.4) driving low-amplitude waves or instabilities. Feature 2 in fig. 2.22 is the magnetic component of the drift-Alfvén wave. The fluctuation power peaks at the gradient region and corresponds with the peak in density fluctuations (fig. 2.8).

Feature 3 is particularly interesting because this the only fluctuating quantity to *increase* with mirror ratio, seen in fig. 2.23. This feature may be broad evanescent Alfvénic fluctuations from the plasma source. These fluctuations have been observed in the LAPD in the source region alongside an Alfvén wave maser [MMC05]. Note that the Alfvén maser cannot enter the mirror cell at mirror ratios greater than 1.75 because the Alfvén maser resonates at $0.57 f_{ci}$ but the midplane is always at or near 500G.

The sub-2 kHz modes in B_{\perp} and its harmonics are nearly constant in power across the entire plasma; these features are likely perturbations from the magnet power supplies and thus ignored. The lack of radial, azimuthal, and axial structure in these magnetic signals below 2 kHz and narrow bandwidth indicate a non-plasma origin. Significant radial and azimuthal structure in B_{\perp} fluctuation power starts to appear in frequencies larger than 4 kHz.

The drift-Alfvénic nature of the 12 kHz Bdot feature is confirmed by changing the flat field from 500G to 400G: the feature shifts down in frequency from 12 to 10 kHz seen in fig. 2.24. From the drift wave and Alfvén wave dispersion relations the frequency is expected to be $400\text{G} / 500\text{G} = 0.8$ of the original, which is approximately what is observed. The k_y of the drift-Alfvén wave also has an effect and may be responsible for a $10\text{ kHz} / 12\text{ kHz} = 0.83$ factor instead.

There may be some sort of resonator made by the mirror cell and its interaction with Alfvén waves. In fig. 2.25, the behavior of the B_{\perp} spectrum in the core changes dramatically between 1 and 10 kHz in the short mirror when compared with the medium and longer mirrors. It's unlikely

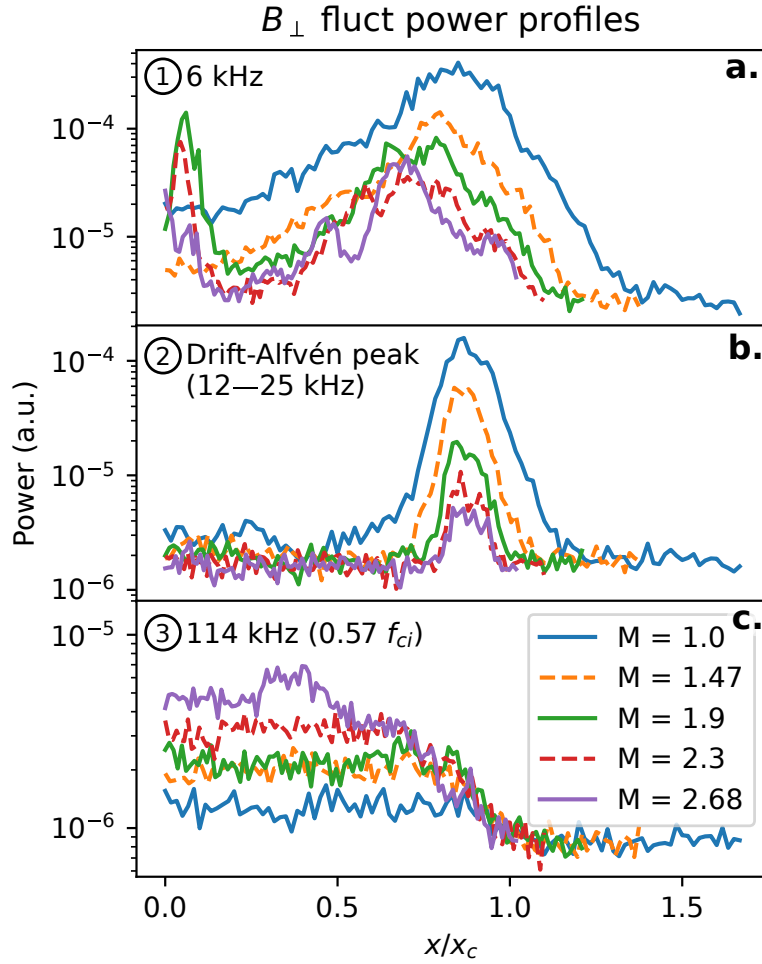


Figure 2.22: B_{\perp} fluctuation power profiles for the three regions shown in fig. 2.21: region 1 (6 kHz) (a), region 2 where frequencies are taken from the peaks of the drift-Alfvén waves for each mirror ratio (b), and region 3 (114 kHz) (c).

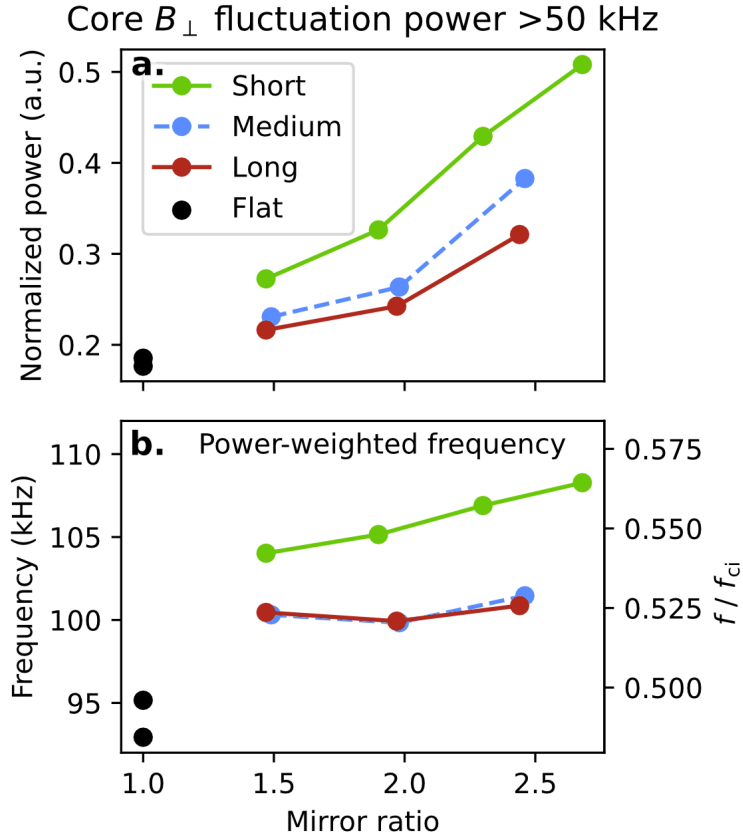


Figure 2.23: Summed fluctuation power of B_{\perp} in the core ($x/x_c \leq 0.3$) as a function of mirror length and ratio. Top (a): the fluctuation power is normalized by the sum of the full-spectrum summed power. Bottom(b): the frequency of the power distribution > 50 kHz weighted by the fluctuation power.

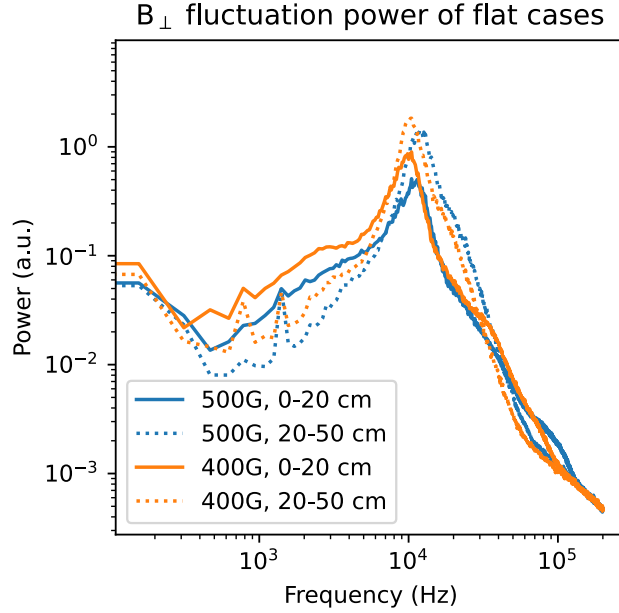


Figure 2.24: B_{\perp} flat field for 500G and 400G flat fields. The frequency of the identified drift-Alfvén wave at 12 kHz drops when the field is lowered, as expected.

that this is an Alfvénic fluctuation because the wavelength is an order of magnitude too large to fit in the machine.

For completeness, B_z fluctuation measurements are seen in fig. 2.26. The peaks in the 10 kHz region are likely crosstalk or slight coil misalignment of the probe and are picking up B_{\perp} fluctuations. The profile low frequency B_z fluctuations can be seen

The low frequency fluctuations in the Bdot spectra may seem important but plotting the spectra as a function of position (fig. 2.27) clearly shows the harmonics of the signal and the narrow bandwidth of them. This spectral feature is present regardless of mirror ratio, but changes in magnitude in approximate proportion with the field, i.e., the magnet power supply current. This power supply-induced field fluctuation can easily be seen in the ≈ 625 Hz mode in B_z , seen in fig. 2.28. The fluctuation power is largely constant across the entire plasma column, with the fluctuation power increasing with increased mirror fields. The taper of the fluctuation power at

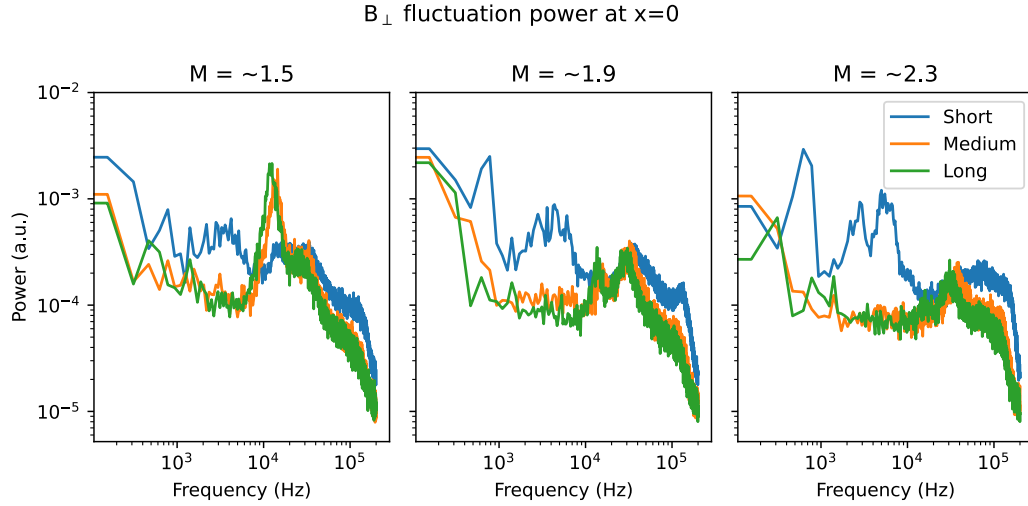


Figure 2.25: B_{\perp} at $x=0$ for different mirror lengths. The origin of fluctuations between 1 and 10 kHz is unknown.

the edge could be caused by the background field vector no longer pointing in the z direction as the probe approaches the magnet coil. In general, the probe valves are not centered between the magnet coils, leading to rotation of the of the field vector as the probe is pulled out.

2.4 2d Structure

The perpendicular magnetic field structure is measured by collecting x-y planar \mathbf{b} dot ($d\mathbf{B}_{\{x,y,z\}}/dt$) data alongside a stationary, axially separated I_{sat} reference probe (DR2). This probe provides a phase reference for the magnetic field fluctuations, allowing a 2d map of relative phase to be constructed over many shots. Only the region around x_{PF} was measured because of constraints on probe movement. The amplitude and phases for each magnetic field component are then used to reconstruct the local magnetic fluctuation vector \mathbf{B} . The axial current density structure, j_z , can be derived from this vector field. \mathbf{B} and the corresponding j_z for the flat-field ($M = 1$) case can be seen in fig. 2.29. Two main current channels can be seen with the magnetic fields circulating around them. This structure quickly decoheres in time as expected in a turbulent plasma. At higher

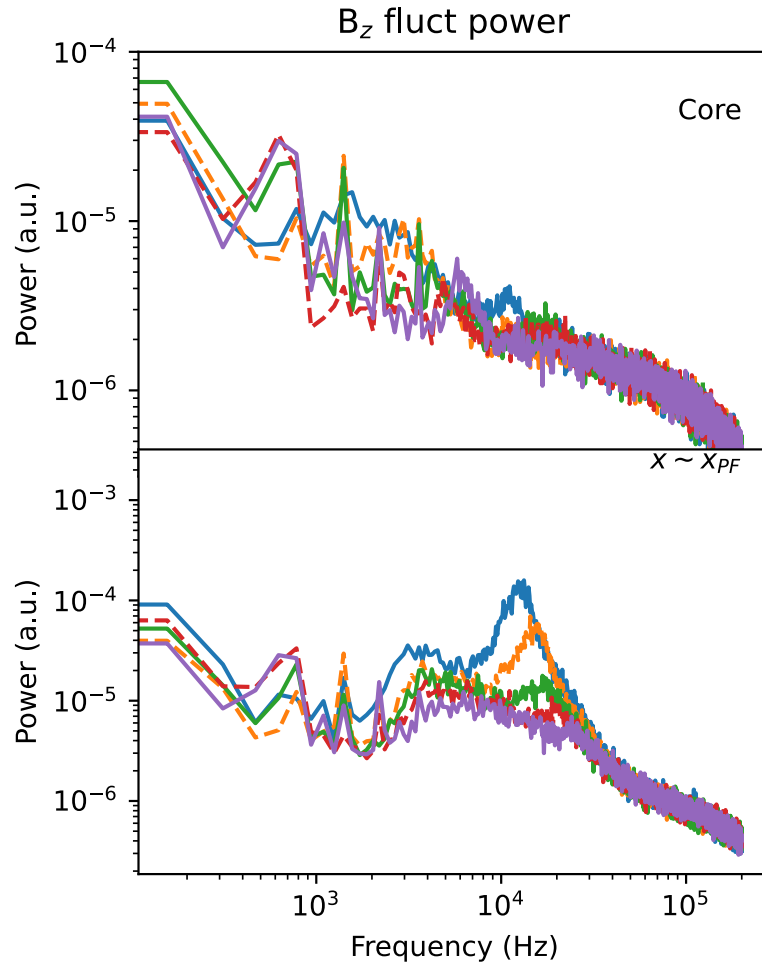


Figure 2.26: B_z fluctuations in the core and x_{PF} . Aside from picking up some B_\perp signal, the spectra are largely featureless.

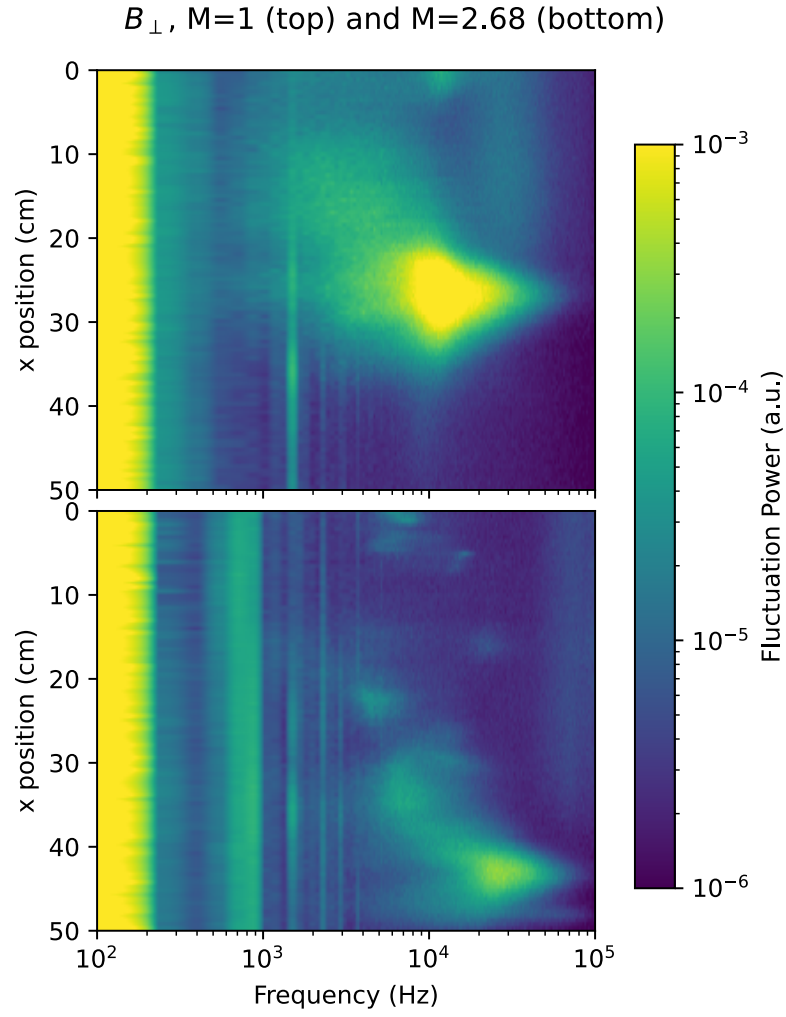


Figure 2.27: B_{\perp} fluctuation power for mirror ratios of 1 and 2.68. Lower frequencies are shown and the colorbar clipped to show detail in what appears to be power supply fluctuations.

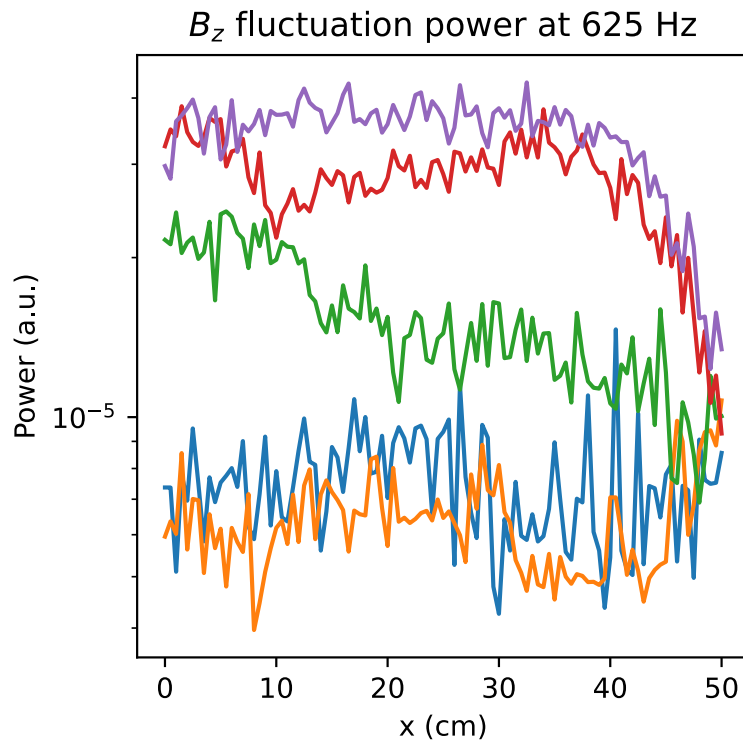


Figure 2.28: B_z fluctuation power profiles for all mirror ratios at 625 Hz.

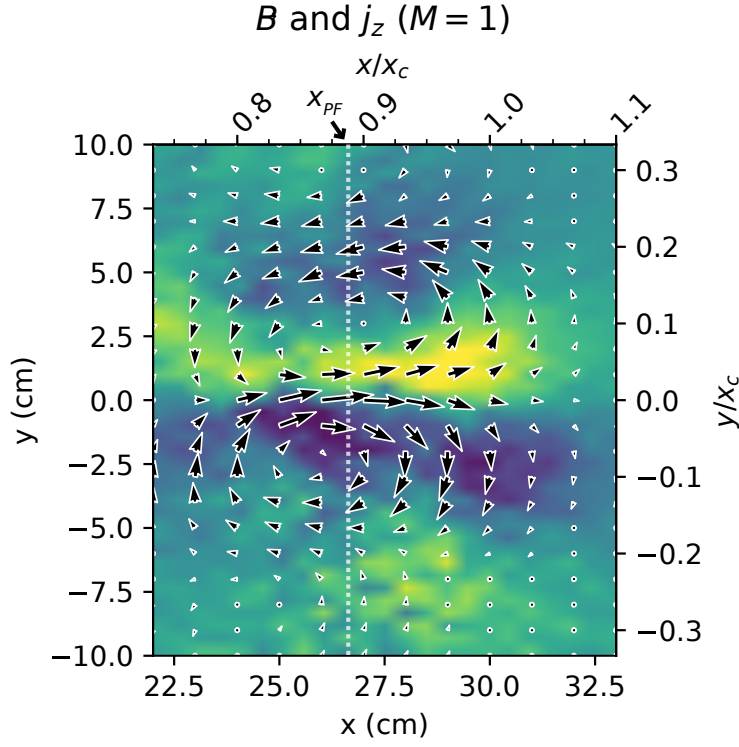


Figure 2.29: Perpendicular magnetic field and the derived current density for the flat-field ($M = 1$) case using a Bdot probe with an axially-separated I_{sat} reference (DR2). The x-y plane was centered near x_{PF} .

mirror ratios, the field magnitude and corresponding current density decrease (which was also seen in DR1: fig. 2.21). Similar structure is seen in the mirror configurations; the $M = 1.9$ and $M = 2.68$ cases can be seen in fig. 2.30.

Using two, axially-separated, correlated I_{sat} measurements (DR2), with one collecting x-y planar data, the azimuthal mode number m (radially integrated) was calculated. Higher-frequency and higher- m features are seen with increasing mirror ratio (fig. 2.31). The increased frequencies may be caused by a change in Doppler shift by the $\mathbf{E} \times \mathbf{B}$ flow. This higher- m trend suggests that azimuthal structures do not scale with increased plasma radius but instead remain roughly the same size. The limited planar probe movement caused an increase in the lower bound on m in higher

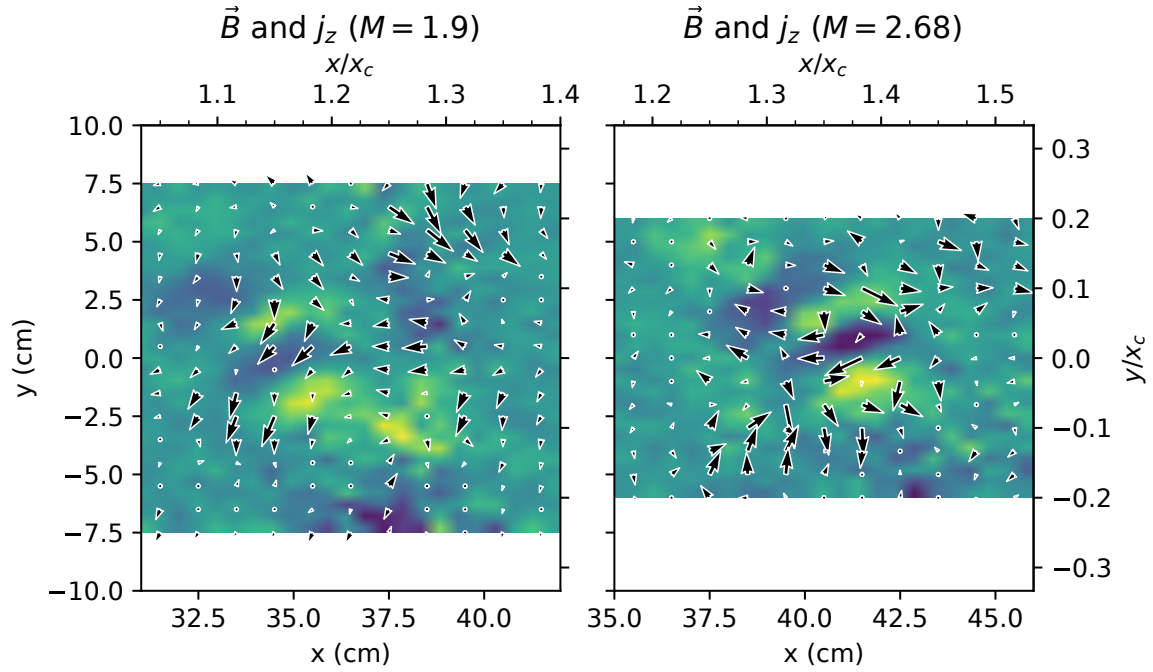


Figure 2.30: Perpendicular magnetic field and the derived current density for the $M = 1.9$ and $M = 2.68$ cases computed in the same manner as fig. 2.29. The x-y planes were centered near x_{PF} , and the view size was kept constant across the plots. The structure is much less obvious in the mirror cases, but all exhibit the expected Alfvén wave pattern

mirror ratios. At mirror ratios 1.47 and higher, the lower frequency component (< 10 kHz) appears to decrease significantly in amplitude. Calculating k_{\perp} from m evaluated at $x \sim x_c$ yields similar k_y values as the two-tip technique (fig. 2.32). The average k_y for a given frequency can be calculated using two Vf tips on the same probe by calculating the phase difference and dividing by the spatial separation of 5 mm: $k_y = \phi_{vf1, vf2} / \Delta y$ [BKP82]. The maximum $|k_y|$ measurable before aliasing is $\pi / \Delta y \approx 628$ rad/m. As seen in fig. 2.32, the k_y spectrum remains similar across mirror ratios, but the wavenumber extends further into higher frequencies with increasing mirror ratio. These azimuthal mode numbers and gradient scale lengths are consistent with linear simulations using the 3d fluid code BOUT [PUC10] in the flat, unbiased case.

2.5 Discussion

2.5.1 Lack of mirror-driven instabilities

No evidence is seen for mirror-driven instabilities curvature, loss-cone, or otherwise. Given the LAPD parameters in this study (tables 2.1 and 2.2), the collision frequencies are sufficiently high such that the mirror is in the gas-dynamic regime: losses out of the mirror throat are governed by gas-dynamic equations rather than free streaming through the loss cone. To be in the gas-dynamic regime, the mirror length must exceed the mean free path of the ions [IP13]:

$$L > \lambda_{ii} \ln M / M \quad (2.2)$$

where L is the mirror length, λ_{ii} is the ion mean free path, and M is the mirror ratio. These collisions populate the loss cone and maintain a (cold) Maxwellian distribution, eliminating the possibility of loss-cone-, ion-driven instabilities like the AIC [CS82] or DCLC [Sim76, Kan79] instabilities that have been observed in other (historic) devices.

The paraxial, approximate interchange growth rate is [Pos87, RBC11]

$$\Gamma_0 = \frac{c_s}{\sqrt{L_M L_P}} \quad (2.3)$$

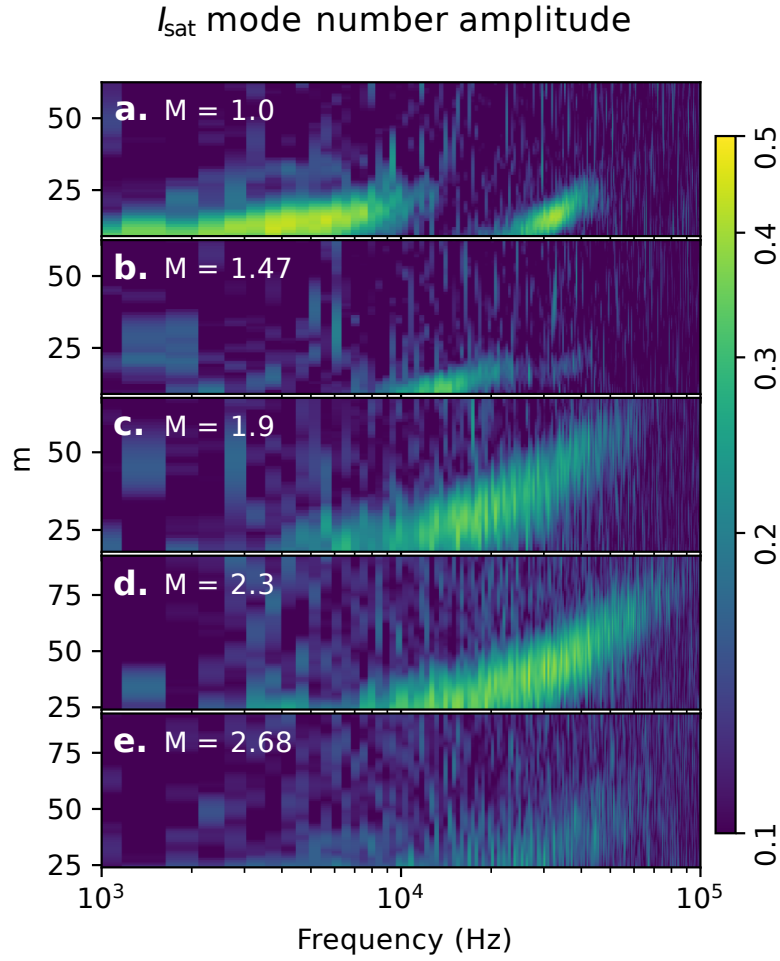


Figure 2.31: Azimuthal mode number m amplitudes calculated from two axially-separated, correlated, I_{sat} probes. Increasing mirror ratio (a to e) leads to increased m at higher frequencies. (DR2)

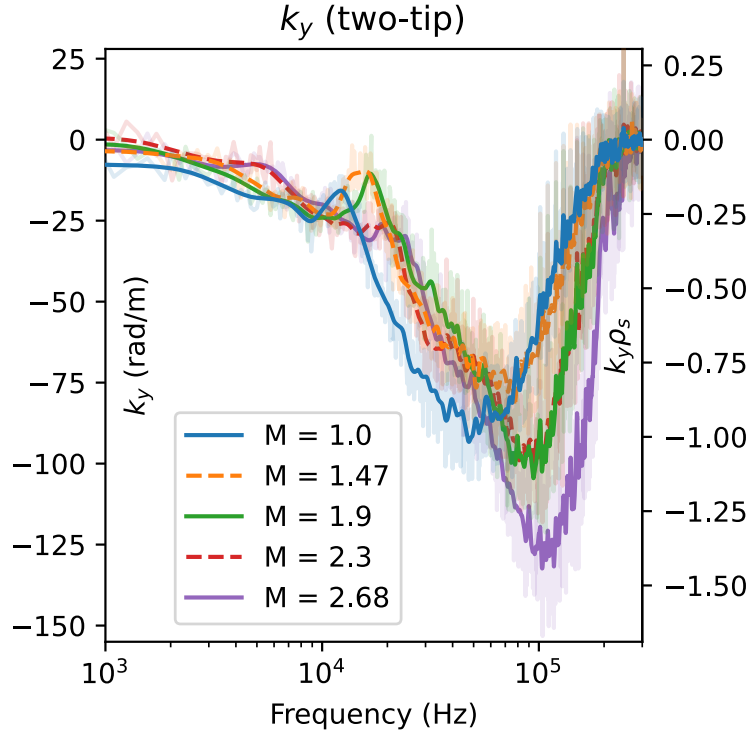


Figure 2.32: k_y averaged about x_{PF} and smoothed for each mirror ratio calculated using two vertically-separated Vf tips on the same probe. Little change is seen in k_y at lower frequencies but higher frequencies tend towards larger k_y at higher mirror ratios.

which yields $\Gamma_0 \approx 1.2$ kHz using $L_M \approx 7$ m and $L_P = 17$ m. c_s is used instead of \bar{v}_i because $T_i \ll T_e$ and mirror length L is split to distinguish between the contributions of the plasma length and mirror length to inertia and to curvature drive, respectively. Interchange is not visible in-part because the aspect ratio of these mirrors is quite large, limiting the growth rate of interchange. The length of the mirror (3.5 m), radius of curvature (6-7 m), and plasma column (17 m) are much larger than the radius of the plasma (0.5 m maximum), so the plasma inertia is large relative to the instability drivers. Line-tying to the cathode may further lower the growth rate. The hot cathode used for plasma formation could function as a thermionic endplate that can supply current to short out the flute-like interchange perturbations. Line-tying has been seen in flux rope experiments on the LAPD using a hotter, denser source [VGP11], also in other devices [FKR79], and is why interchange was not seen in the earliest mirror machines [Pos87]. Note that the plasma terminates on the cathode or end plates before the magnetic field flares out, so there is no contribution to stability from an expander tank as seen in other GDTs [RBC11, IP13]. Finite Larmor radius (FLR) effects may provide a stabilizing effect for larger azimuthal mode numbers. At the highest mirror ratio, assuming a plasma radius of $a_0 = \sqrt{2.68} * x_{PF} = 43$ cm, the FLR stability criterion $\frac{m}{2} \frac{\rho_i L}{a_0^2} > 1$ [RBC11] suggests a stabilizing effect may be present for azimuthal mode numbers $m > 4$.

If the curvature-induced interchange instability were observable, then introducing a mirror configuration would lead to new features in I_{sat} and B_{dot} fluctuations. In particular, low-frequency mode(s) – likely less than 10 kHz given the low m-number and plasma rotation rates – would be observed growing from the pressure gradient region. For onset of the interchange instability, the mirror curvature or plasma pressure would need to be increased but the precise conditions required for this onset are not yet known for the LAPD.

Interchange could also be at least partially stabilized by the continuous production of electrons in the core that are electrostatically trapped by the ambipolar potential [GH71]. The intuition behind this stabilization mechanism is as follows: electrons are continuously produced via ionization of neutrals, and any change in the local potential will cause more or fewer electrons to be lost out the ends of the device along that field line, counteracting the potential change. This stabilization

mechanism has been experimentally demonstrated to completely suppress interchange when the ambipolar potential $\Phi \gtrsim 6T_e$ [KHS87].

The $\mathbf{E} \times \mathbf{B}$ shear flow present (fig. 2.7) may also make a contribution to the stabilization of interchange [RBC11, BLZ03, BBS07, BBC10]. The estimated shearing rate is between 3 and 10 kHz, which is greater than the estimated ≈ 1.2 kHz growth rate of the interchange mode.

2.5.2 Instabilities driving LAPD turbulence

Rotational interchange can be significant driver of the broadband turbulence spectrum in the LAPD, particularly when a biased limiter is installed. This observation has been confirmed by both linear simulations [PUC10] and biasing experiments [Sch13].

This rotational interchange mode has the following attributes, as summarized by [Jas72]: flute-like ($k_{\parallel} = 0$), $|e\tilde{\phi}/T_e|/|\tilde{n}/n| \gtrsim 1$, radial potential phase variation 45 to 90°, maximum possible $|e\tilde{\phi}/T_e| < 1$. All of these attributes are seen for the lower frequency (3 kHz) mode. The Vf radial phase variation when $M > 1$ is not clearly seen because the coherency is dramatically reduced along the field line. The rotational interchange mode could couple with the drift wave at $k_{\parallel} = \pi/L \sim 0.37$ rad/m ($n = 0.5$), which has been observed in the past [Sch13] and likely present here. Estimates of shearing rate from the $\mathbf{E} \times \mathbf{B}$ flow velocity profile (fig. 2.7), calculated fluctuation ratios, and radial phase shift variation suggest that Kelvin-Helmholtz-driven turbulence is not significant, if present at all. Historically, biasing a limiter has been required to clearly observe the Kelvin-Helmholtz instability [HPC05, SCR12, Sch13].

Low frequency density fluctuations may also be driven by a flute-like conducting-wall temperature-gradient instability which only requires an electron temperature gradient to grow (even with straight field lines) [BRT91]. Simulations of turbulence in the LAPD suggest the possible presence of these conducting wall modes (CWM) which have the highest growth rate for $m \leq 20$ [FCU13]. This lower- m mode could be responsible for the peak around 3 kHz in the $M = 1$ I_{sat} fluctuation (fig. 2.16) and azimuthal mode numbers (fig. 2.31) and for the low-frequency low- k_{\parallel} or flute-like

behavior (fig. 2.17). This CWM may also be responsible for flatter electron temperature profiles seen in previous studies [PMC22, Sch13] (fig. 2.6).

These linearly unstable modes may be outgrown by a rapidly-growing nonlinear instability that couples to drift-like modes as suggested by simulations [FCU13]. This nonlinear instability is driven by the density gradient at an axial modenummer of $n = 0$ and nonlinearly transfers energy to $n \neq 0$ fluctuations.

The conducting wall mode and nonlinear instability may be present in these mirror experiments but the spectra are adequately explained by linearly unstable modes. Precise identification these modes requires further study; neither of these instabilities have been directly observed in the LAPD.

2.5.3 Causes of particle flux reduction

The reduction in particle flux explained by a reduction in density fluctuations likely caused by a increased gradient scale length $L_n = \frac{n}{\nabla n}$ (fig. 2.33), decreasing the linear drift wave growth rate and saturation level seen in sec. 2.3.5. This gradient length reduction may also reduce the growth rate of the rotational interchange instability, which may be the dominate driver for the low-frequency large-amplitude density fluctuations. The influence of this density fluctuation reduction appears reduced at higher mirror ratios past $M = 1.9$, where the wavenumber and phase angle appear to decrease in magnitude. The plot showing this breakdown in particle flux can be seen in fig. 2.34. The changes in I_{sat} fluctuation power is the most obvious driver, but the I_{sat} - V_f phase difference, coherency and wavenumber also seem to have an effect. The V_f fluctuation power remains largely consistent across the different mirror ratios. Note that this particle flux appears somewhat different because this is using the uncalibrated I_{sat} values and the flux is not scaled by solid angle. This flux also does not use temperature-compensated I_{sat} measurements.

The decorrelation time of I_{sat} time series data is around 0.15 ms at x_{PF} . An estimate of the $\mathbf{E} \times \mathbf{B}$ flow shear from fig. 2.7 (DR2) yields a shearing time between 0.1 and 0.3 ms at x_{PF} . These

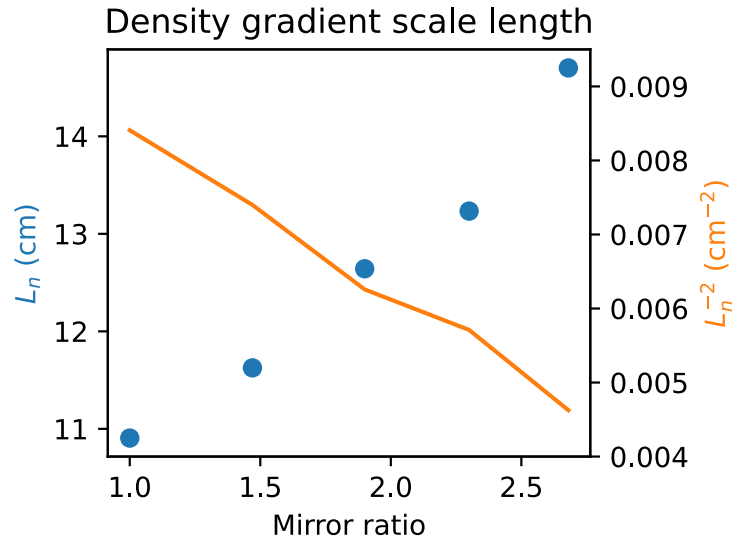


Figure 2.33: Gradient scale length L_n and the associated term in the drift wave growth rate L_n^{-2} . This scale length was calculated over a 3 cm region around x_{PF} (peak fluctuation region) at the mid-plane. Increasing the mirror ratio increases the gradient scale length, which suggests weakening of the underlying instability driver.

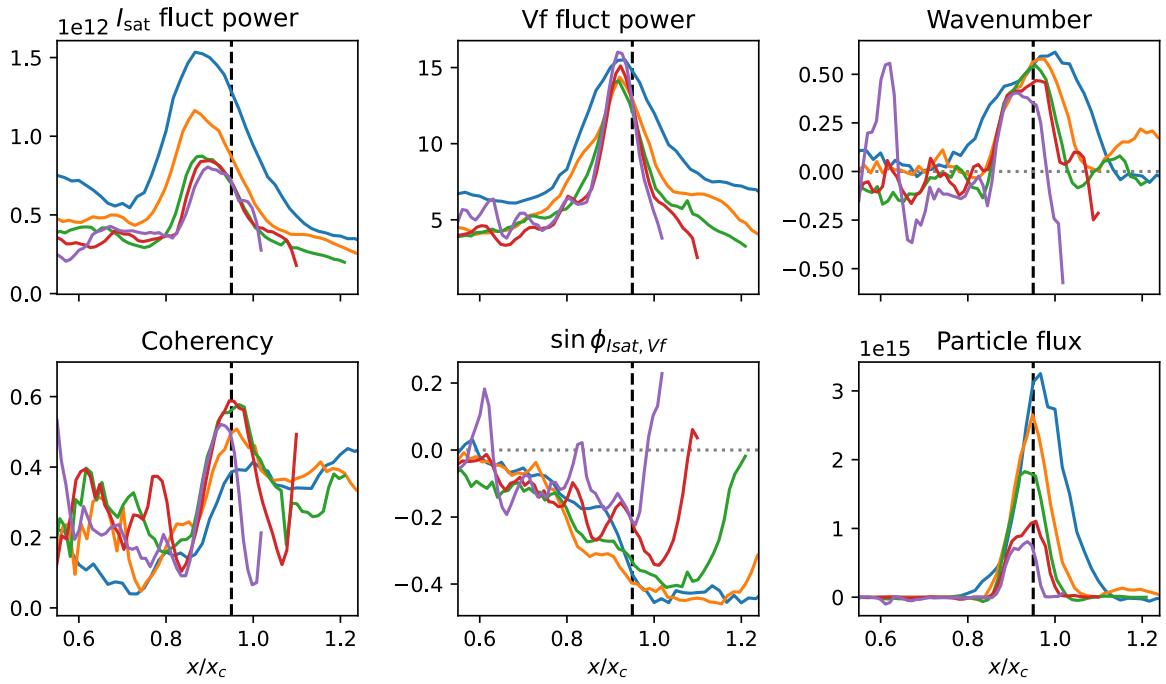


Figure 2.34: The particle flux broken down into the components used to calculate it. The dashed black line is simply a visual reference near the peak particle flux at $x/x_c = 0.95$. The I_{sat} fluctuation power appears to be the largest driver in changes in particle flux. The colored lines correspond to mirror ratio as seen in earlier plots.

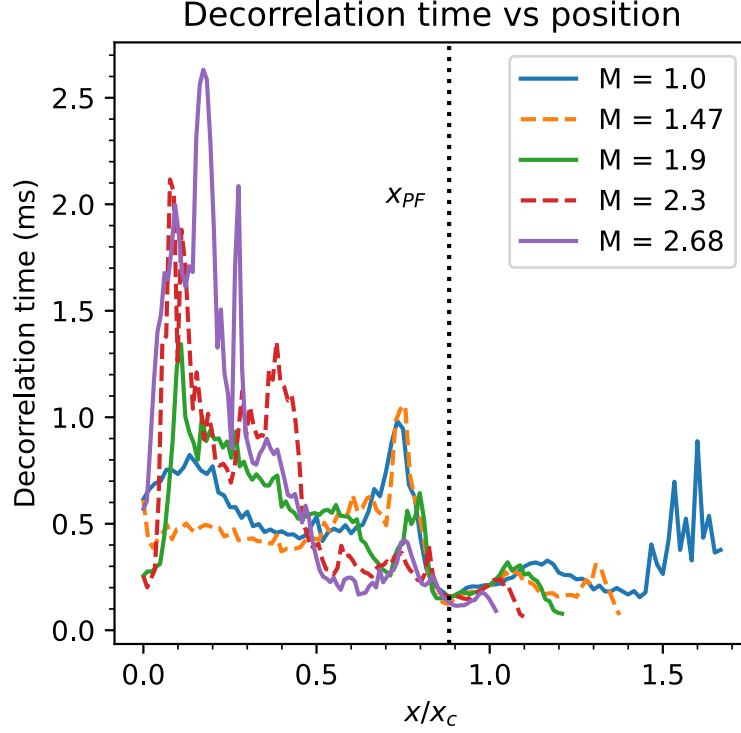


Figure 2.35: Decorrelation time from I_{sat} time series data for different mirror ratios. All of the mirror ratios have a minimum decorrelation time at x_{PF} and much longer times (slower rate) in the core.

times suggest that spontaneous flow shear may be important for suppressing turbulence, as seen in other studies [SCR13, CYK05], at all mirror ratios. However, no clear trend in shearing strength is seen with mirror ratio.

The decorrelation time of a signal is calculated by taking the autocorrelation of a signal – I_{sat} in this case – and finding the full-width half-max of the envelope using a Hilbert transform. This decorrelation time can be seen in fig. 2.35. The decorrelation is minimized at x_{PF} and maximized in the core, further confirming the turbulent nature of the fluctuations at x_{PF} .

The estimated shearing rate from DR2 can be seen in fig. 2.36. The rate is plotted instead of time because of the singularity when the flow reverses. At around x_{PF} ($x/x_c \approx 0.87$), the shearing

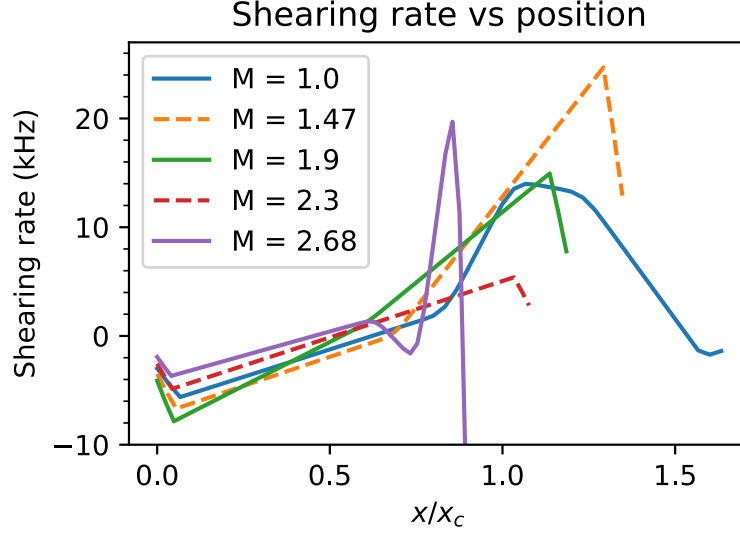


Figure 2.36: ExB shearing rate based on smoothed plasma potential profiles. This shearing rate is comparable to the decorrelation rate at x_{PF} , seen in fig. 2.35.

rate is around 2 to 8 kHz meaning the shearing time is around 0.5 to 0.125 ms. This is fairly close to the decorrelation time from the I_{sat} time series measurements (fig. 2.35). These similar times/rates suggests that ExB shearing may set the limit on cross-field transport.

It is important to note that the electron thermal diffusion time along the field line is very long compared to the frequency of the drift wave ($\omega \gtrsim k_{\parallel} \bar{v}_e^2 / v_{ei}$) [Gol95] so the electron temperature along the field line may not be constant on the drift wave timescale. This factor is not taken into account in this analysis but may have substantial impact on interpretations of the measured phase shift.

2.5.4 Differences between DR1 and DR2

Directly applying signals between these two dataruns is not quite appropriate because the profiles/plasmas changed appreciably. These changes could have been caused by differences in cathode temperature, emissivity, or other properties. The discharge power for DR2 was roughly 10%

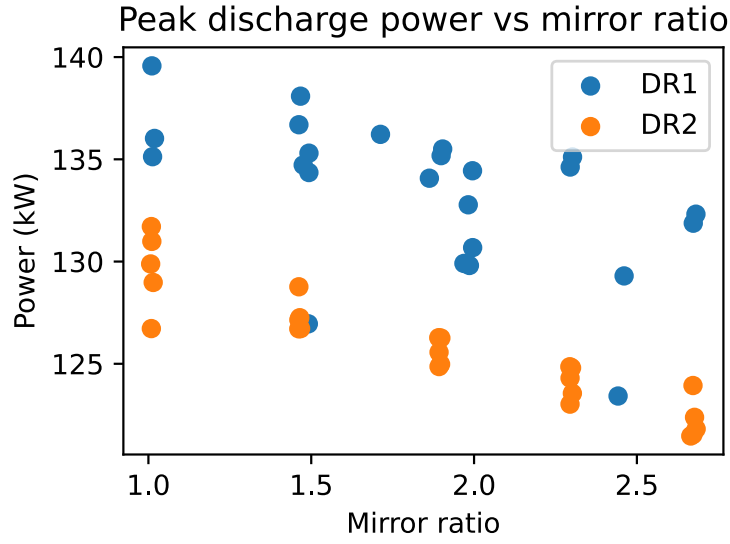


Figure 2.37: Discharge power vs mirror ratio. DR2 had roughly 5% lower discharge power than in DR1 for unknown reasons.

smaller than what was seen in DR2 seen in fig. 2.37. Since the discharge voltages were similar (DR1: 62.5 vs DR2: 60.5) we expect to see less dense plasmas in DR2.

Changes in the I_{sat} profiles between the two dataruns (and between two separate measurements in DR1) can be seen in fig. 2.38. Interestingly, there is some difference in the profiles *within the same datarun* which could be caused by probe shadowing. Probe shadowing effects should be less important in mirrors because the probe closest to the cathode magnetically maps to a region further outside than the probes in the mirror cell. This difference in density can also be seen in the line-integrated density from the 56 GHz interferometer (port 23): fig. 2.39. These differences in density could also be caused by different hydrogen and helium pressures in the runs. Helium pressure was roughly the same for both dataruns (6e-6 to 3e-6 for DR1, 6e-6 to 2e-5 for DR2), but the hydrogen pressure was an order of magnitude higher for the DR2, on the order 7e-6 instead of 1e-7 for DR1. These differences in pressures could have had an effect on plasma formation and transport, thus affecting profiles. Hydrogen fraction is known to have an effect on breakdown characteristics in the newer Lanthanum-hexaboride (LaB6) cathode.

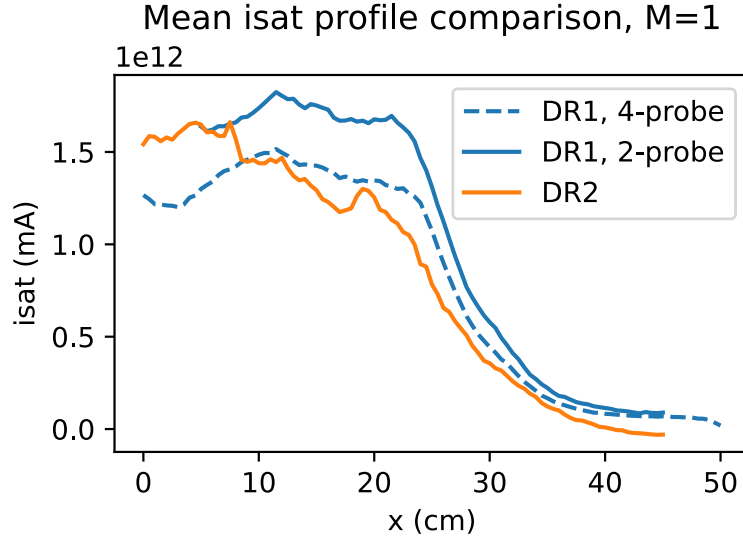


Figure 2.38: I_{sat} profiles (M=1), DR1 vs DR2 in the mirror cell. DR2 has reduced I_{sat} across the entire profile. Identical machine settings in DR1 a few days apart are also different.

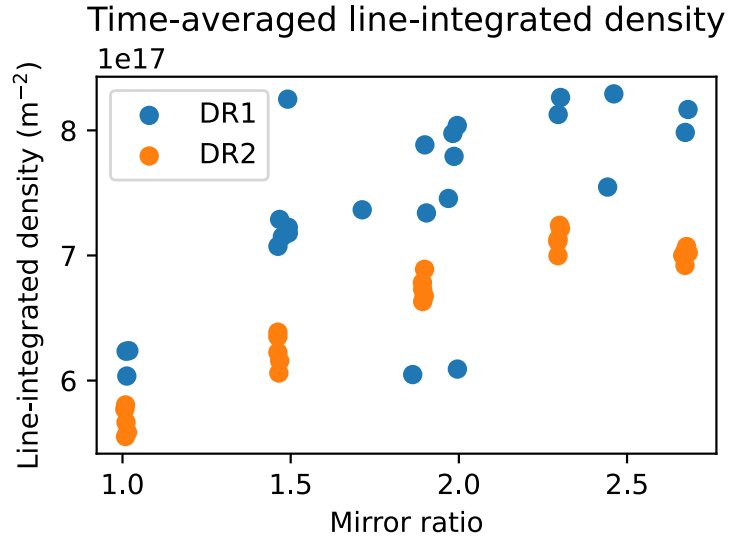


Figure 2.39: Line integrated density from the 56 GHz, DR1 vs DR2. On average, DR2 has a lower density than what's seen in DR1. The interferometer is located near the region of good curvature closest to the cathode.

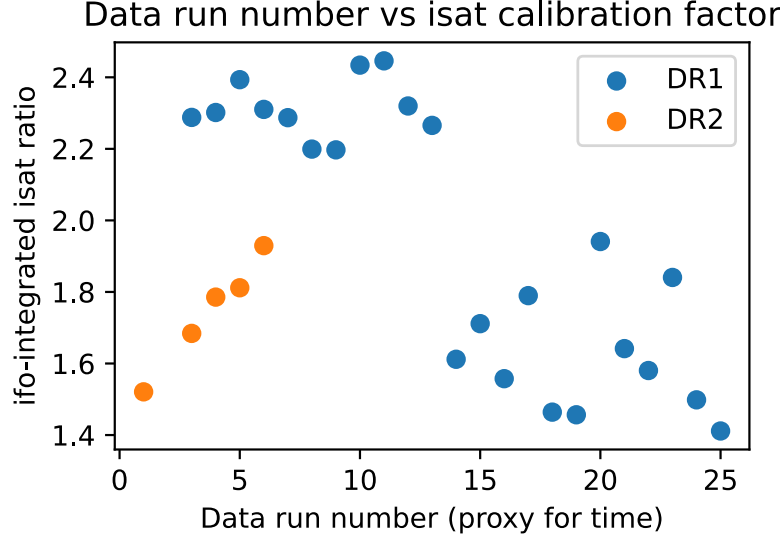


Figure 2.40: I_{sat} calibration factor over different dataruns from the same run sets. Datarun number is monotonically increasing, so in this case it's used as a proxy for time. A rather large variance is seen in this calibration factor, which suggests the I_{sat} probes having time-varying characteristics affecting the measurement.

Differences could also occur within dataruns. Calibrating the effective area of the I_{sat} probes can be done using the 56 GHz interferometer, but this calibration factor drifted over time and seen in fig. 2.40. This could be deposits being removed or added to the probe, affecting the effective area. This calls into question the reliability of absolute I_{sat} measurements, but we proceed regardless because there's no easy way to fix this issue.

2.6 Conclusions and future work

Turbulence and transport was studied in mirrors with varying lengths and ratios using the flexible magnetic geometry of the LAPD. Particle flux and fluctuation amplitudes decreased up to a factor of two when mirror ratio was increased. The primary drivers of turbulence were identified as the rotational interchange mode, caused by spontaneous rotation, and unstable drift-Alfvén waves

driven by the density gradient. The decrease in density fluctuation amplitudes can be attributed to an increase in the gradient scale length caused by the dimensionally wider plasma at the mirror midplane. Despite imposing a mirror configuration, no signs of mirror-driven instabilities were observed. The highly-collisional, GDT-like plasma produced suppressed any velocity space instabilities. The interchange growth rate was likely suppressed to an undetectable level by line-tying, in-cell electron production, and shear flow.

Future experiments in hotter regimes with the new LaB6 cathode [QGP23a] will need to be performed to evaluate the robustness of these results, particularly concerning the stabilization of curvature-induced interchange. Additionally, the source field should be matched to the mirror midplane field so that the plasma remains the same radius to isolate geometric effects. Simultaneous measurements using flux and/or vorticity probes and I_{sat} are needed to concretely determine if azimuthal flow shear is modified by the mirror field, and to quantify the effect of flows on rotational interchange and drift wave instability drive in general. Multiple simultaneous axial measurements of potential would enable better understanding of the axial wavenumber and identification of possible modes.